Department of Physics and Astronomy
Heidelberg University

Bachelor Thesis in Physics
submitted by

Ellen Bräutigam

born in Weimar (Germany)

2022

Construction of an Airborne Chemiluminescence Ozone Monitor for Volcanic Plumes

This Bachelor Thesis has been carried out by Ellen Bräutigam at the

Institute for Environmental Physics (IUP) in Heidelberg

under the supervision of

Prof. Ulrich Platt

Abstract

Ozone plays an important role in volcanic plume chemistry, a particular process is its destruction by reactive halogen species, especially BrO. To better understand this chemical system, further measurements of the ozone concentration in volcanic plumes are needed. The usual UV absorption ozone monitors suffer from a severe interference with the high SO_2 concentration in volcanic plumes. Therefore, we use the chemiluminescence method, which is based on the detection of photons emitted when ethylene is mixed with ozone containing air. This method has no interference with volcanic plume components, but its field deployability is so far very limited, because the instruments are typically very heavy and bulky.

This thesis reports the construction of a lightweight ($< 1.5\,\mathrm{kg}$) chemiluminescence ozone monitor, that can be mounted on a drone to be carried through volcanic plumes. The weight reduction was mainly achieved by using a modern photomultiplier module and omitting its cooling. In addition, the battery and ethylene storage container are easy to exchange between flights. This means that they can be quite small, as they only need to last for one flight. The flow rates and the dimension of the reaction chamber are optimized based on the calculation of the photon rate and a simulation of the photon trajectories.

Zusammenfassung

Ozon spielt eine wichtige Rolle in der Chemie von Vulkanfahnen, vor allem weil es durch die Katalyse von reaktive Halogenverbindungen, insbesondere BrO, zerstört wird. Um dieses chemische System besser zu verstehen, sind weitere Messungen der Ozon-Konzentration in Vulkanfahnen erforderlich. Die übliche UV-Absorptions-Messmethode hat signifikante Interferenzen durch die hohen SO_2-Konzentrationen in Vulkanfahnen. Daher verwenden wir Chemilumineszenz-Ozonmonitore, welche auf der Reaktion von Ozon mit Ethen basieren. Solche Geräte weisen keine Interferenz mit Vulkangasen auf. Allerdings sind sie normalerweise sehr groß und schwer, sodass Messungen am Vulkan nur sehr eingeschränkt möglich sind.

In dieser Arbeit wird ein leichter ($< 1.5\,\mathrm{kg}$) Chemilumineszenz-Ozonmonitor gebaut, der auf einer Drohne montiert und durch die Vulkanfahne geflogen werden kann. Die Gewichtsreduzierung wurde hauptsächlich durch die Verwendung eines modernen Photomultiplier-Moduls und den Verzicht auf dessen Kühlung erreicht. Außerdem lassen sich der Akku und die Ethen-Gasflasche zwischen Messflügen leicht austauschen. Da sie somit nur für einen Flug reichen müssen, können sie sehr klein und leicht sein. Auf der Grundlage von Berechnungen der Reaktionsrate und der Simulation von Photonenflugbahnen werden die Größe der Reaktionskammer und die Flussraten von Ethen und Luft optimiert.

Contents

1 Introduction

1.1 Ozone and Volcanic Plume Chemistry

Many active volcanoes permanently emit a large variety of gases and aerosols, not only during eruptive phases. As the volcanic plume mixes with ambient air and is exposed to light, a complicated and unique chemical system evolves.

Understanding the chemistry in volcanic plumes is essential for understanding the volcano and its magmatic system (e.g. Burton et al. 2007). Observing the gas emission can be part of volcanic monitoring, because the composition of the emitted gas is often linked to the volcano's activity. Furthermore, it is important to examine the impact of volcanic gases on the chemistry of the atmosphere, as they are a major source of reactive chemical species (von Glasow et al. 2009).
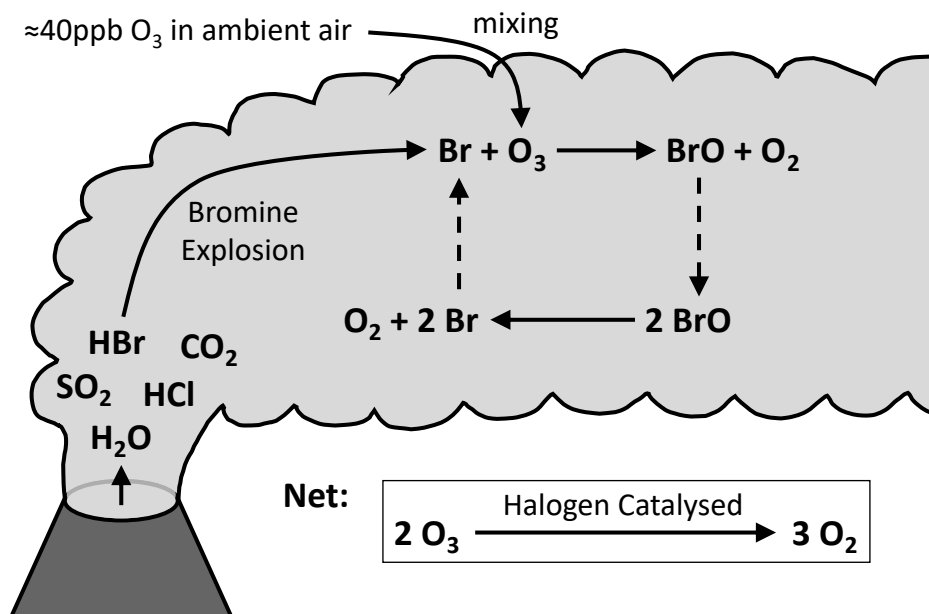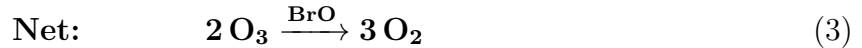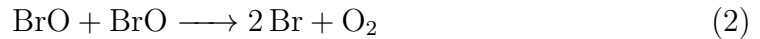

Figure 1: Bromine chemistry in volcanic plumes: Initially emitted HBr is converted to reactive bromine species through the 'bromine explosion'. Catalytic cycling between Br and BrO then sustains destruction of ozone from the atmospheric background.

The emissions mainly consist of water vapour (H_2O), carbon dioxide (CO_2), and sulfur dioxide (SO_2), but there is also a significant amount of reactive halogen species like hydrogen chloride (HCl) and hydrogen bromide (HBr) (e.g. Platt and Bobrowski 2015). As the ambient air mixes into the plume and if light is present the hydrogen bromide is converted to atomic bromine (Br) very rapidly. This chemical process is called the 'bromine explosion' (Platt and Lehrer 1996; Gutmann et al. 2018, p. 9).

With the ambient air also ozone (O_3) is mixed into the plume. Bromine atoms are oxidized by ozone, becoming BrO (reaction 1). It then recycles itself by the BrO self reaction (reaction 2) (Gutmann et al. 2018, p. 11). Overall, ozone is converted into oxygen (O_2) by a bromine catalyzed reaction cycle (see Fig. 1).

$$\text{Br} + \text{O}_3 \longrightarrow \text{BrO} + \text{O}_2 \tag{1}$$

$$\text{BrO} + \text{BrO} \longrightarrow 2\,\text{Br} + \text{O}_2 \tag{2}$$

$$\textbf{Net:} \qquad \mathbf{2\,O_3 \xrightarrow{\ \text{BrO}\ } 3\,O_2} \tag{3}$$
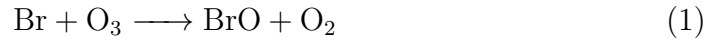
1.1.1 Theoretical calculation of the Ozone Budget

In volcanic plume conditions the BrO self reaction (2) is frequently rate determining in this reaction cycle (Rüth 2021, p. 12). In this case, the ozone destruction rate can be estimated by

$$\frac{d[\text{O}_3]}{dt} \approx -2 \cdot k_{\text{BrO}+\text{BrO}} \cdot [\text{BrO}]^2$$

With $k_{\text{BrO}+\text{BrO}} = 2.7 \cdot 10^{-12} cm^3 s^{-1}$ as the reaction constant of the BrO self reaction (Atkinson et al. 2000) and [O_3] and [BrO] the concentrations of ozone and BrO. The factor 2 expresses that for each BrO self reaction two bromine atoms are formed, which in turn can each destroy an ozone molecule. With a relatively high, but often observed BrO concentration of (e.g. Bobrowski et al. 2007)

$$[\text{BrO}] = 400\,\text{ppt} \,\hat{=}\, 10^{10}\ \text{cm}^{-3} \quad \text{(at 1 bar, 25 °C)}$$

the ozone destruction rate is

$$\frac{d[\text{O}_3]}{dt} \approx -5.4 \cdot 10^8\,\text{cm}^{-3}\,\text{s}^{-1}$$

At this rate the typical amount of ozone in ambient air (Gaudel et al. 2018)

$$[\text{O}_3] = 40\,\text{ppb} \,\hat{=}\, 10^{12}\ \text{cm}^{-3} \quad \text{(at 1 bar, 25 °C)}$$

is destroyed in about 30 minutes. Based on this result, one could expect an ozone depletion inside volcanic plumes.

However, volcanic plumes are subject to turbulent diffusion in the atmosphere, leading to a constant in-mixing of ambient ozone. The ozone concentration inside the plume, thus, can be estimated very roughly by considering the equilibrium state between the destruction of ozone inside and the replenishing flow from the outside. Figure 2 shows, how the volcanic plume is modeled.
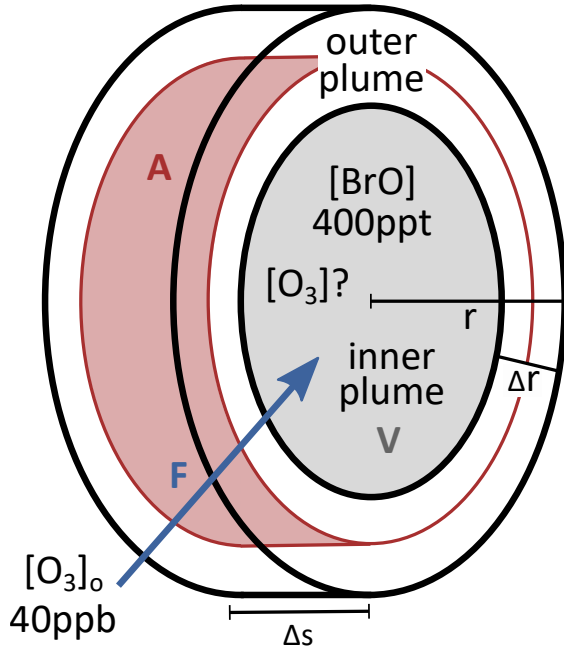
Figure 2:

The volcanic plume is modeled as a slice with radius r and width Δs. It is divided into an inner plume with volume V and an outer plume with a width Δr. The border of the plume with surface A lies in the middle of the outer plume. A total flow F of ozone reaches the inner plume through this surface. There are 400 ppt BrO in the inner plume and 40 ppb ozone outside the plume. The value in question is the concentration of ozone inside the plume.

Fick's first law is used to calculate the ozone flux through the outer plume. The values inserted in the following correspond to a relatively young plume, only a few minutes old.

$$\text{total destruction rate} = \left|\frac{d[O_3]}{dt}\right| \cdot V \overset{!}{=\!=} K_t \cdot \frac{\Delta[O_3]}{\Delta r} \cdot A = \text{total flow} F$$

with radius of total plume $r = 50\,\text{m}$

width of slice $\Delta s = 10\,\text{m}$

width of outer plume $\Delta r = 20\,\text{m}$

volume of inner plume $V = \pi \cdot (r - \Delta r)^2 \cdot \Delta s = 3 \cdot 10^{10}\,\text{cm}^3$

surface of the plume $A = 2\pi \cdot (r - \Delta r/2) \cdot \Delta s = 2.5 \cdot 10^7\,\text{cm}^2$

ozone destruction rate $\frac{d[O_3]}{dt} \approx -5.4 \cdot 10^8\,\text{cm}^{-3}\,\text{s}^{-1}$ (from above)

total destruction rate $\frac{d[O_3]}{dt} \cdot V = -1.5 \cdot 10^{19}\,\text{s}^{-1}$

turbulent diffusion constant $K_t = 10\,\text{m}^2\,\text{s}^{-1}$

$$\implies [O_3]_{out} - [O_3]_{in} = \Delta[O_3] = \frac{d[O_3]}{dt} \cdot \frac{V \cdot \Delta r}{K_t \cdot A} = 1.2 \cdot 10^{10}\,\text{cm}^{-3} \mathrel{\hat{=}} 0.5\,\text{ppb}$$

$$\implies \text{relative depletion} = \frac{\Delta[O_3]}{[O_3]_{out}} = 0.012 = 1.2\,\%$$

This calculation shows, that even if one assumes a high BrO concentration, the ozone depletion inside the young plume should be negligible, because the ozone replenishes faster from the outside than it can be destroyed by the BrO cycle.

The considerations in this chapter are adapted from Rüth (2021) chapter 3. More elaborate calculations regarding this can be found there.

1.1.2 Available Ozone Measurement Techniques

There is a huge interest in ozone, because of its chemical and radiative importance in the atmosphere. Therefore, there is a wide range of techniques to measure ozone concentration in the ambient air (e.g. Parrish and Fehsenfeld 2000, chapter 3.1.1).

Nowadays most commonly used and commercially available are short path UV absorption monitors, because of their easy usage and low maintenance. But cross sensitivities make them unsuitable for usage in volcanic plumes, as will be discussed in section 1.2.

Another option are electrochemical devices. The ambient air containing ozone is brought into contact with a solution. The chemical reactions than cause an alteration of the electric conductivity of the solution, which can be measured. These monitors can be light and cheap and are used to measure vertical ozone profiles of the atmosphere. However, they suffer from interference with other compounds and have a relatively low sensitivity compared to the other options.

There are also several methods based on chemical reactions between ozone and a reactant, that create chemiluminescent (CL) molecules. These emit photons, which are then measured with a photomultiplier to draw conclusions about the ozone concentration. The reactant can be a organic dye (e.g. eosin) that can be solved in a liquid (wet CL) or applied on a surface (dry CL) (Zahn et al. 2012). Another possibility are gas phase reactions with nitrogen monoxide (NO) or unsaturated hydrocarbons. Foremost among these chemiluminescence methods is the usage of ethylene (C_2H_4) as the reactant. Such monitors were commercially available in the 1970s and 1980s, before the UV absorption monitors arose. It is also the method used by the ozone monitor constructed in this thesis.

1.1.3 Former Experimental Studies of Ozone in Volcanic Plumes

Table 1 compiles the results and setups of former studies that measured ozone depletion in volcanic plumes. The reported values show great variation, with everything from no depletion up to 90% depletion.

This is caused by the dependence of ozone chemistry on the volcano and its emission phases, the age of the volcanic plume (distance from the crater, time since emission) and ambient conditions among other factors. It is still not clear what happens to ozone inside volcanic plumes.

However, this knowledge is crucial to validate chemical models, because ozone, as a reactive species, plays an important role. It is also needed to interpret BrO measurements correctly, since ozone and BrO are closely related. BrO concentrations in volcanic plumes are known relatively well, because they can be measured by remote sensing techniques (e.g. MAX-DOAS (e.g. Bobrowski et al. 2007), satellites (e.g. Wagner and Platt 1998)). Moreover, the contradiction between the measurements in table 1 and the calculations in section 1.1.1 has to be resolved.

This shows the need for reliable and more plentiful measurements of ozone in volcanic plumes.

location	measurement platform	instrument type	relative ozone depletion [%]	remarks	reference
Etna	ground based	UV absorption (2B Technologies, model 202)	15-45	Use of two CrO3 scrubbers in series	(Surl et al. 2015)
Augustine (1976)	airborne	CL (Monitor Labs model 841ßA, ethylene)	average: 60	Large variability (0-100), plume aged several hours	(Vance et al. 2010)
Etna (2004, 2009)	ground based	UV absorption (2B Technologies)	15-40	Use of CrO3 scrubber, depletion within in tens of seconds from crater	(Vance et al. 2010)
Eyjafjallajökull (2010)	airborne	UV absorption (dual cell, Thermo Environmental Instruments Inc. Models 49C)	4-84 (per transect)	Mean: 47 standard deviation: 21, depletion maintained in 1-9 days old plume, strong anti correlation with SO2	(Vance et al. 2010)
Kilauea	ground based	Electrochemical (Aeroqual instrument, WO3 sensor)	no depletion	Kilauea is a low halogen emitter	(Roberts 2018)
Sakurajima	ground based	UV absorption (Thermo Environmental instrument, model 49)		Rapid decrease of O3 for increase in SO2	(Lee et al. 2005)
Redoubt (2010)	airborne	UV absorption (2B Technologies, Inc., Model 205)	80	Data post processing; entertainment of ambient air and chemical O3 loss have to be separated; chemical loss: 1-16 ppb	(Kelly et al. 2013)
St. Helens (200km downwind)	airborne	unknown	33-70		(Fruchter et al. 1980)
St. Helens (33km downwind)	airborne	CL (Monitor Labs model 8410A, ethylene)	max. 90	Depletion for phreatic emissions, no depletion for paroxysmal or intra-eruptive emissions	(Hobbs et al. 1982)
Mt. Erebus (2005)	airborne	UV absorption	35	Depletion only observed when SO2 exceeds 20 ppb	(Oppenheimer et al. 2010)
Tungurahua (Ecuador)	airborne	CL (FastOz, Nitric Oxide)	20-30	Data insufficient to attribute all depletion to chemical reactions	(Carn et al. 2011)

Table 1: Compilation of measurements reporting O3 depletion. The approaches taken to measure the O3 depletion as well as their actual values vary greatly. (from Rüth (2021) table 1; based on Surl et al. (2015))

1.2 SO₂ interference of UV Absorption Monitors

Nowadays the standard method to measure ozone concentration are short path ultraviolet (UV) absorption monitors. These are also employed by the majority of studies in table 1. The measurement principle is explained in figure 3 (Rüth 2021, chapter 4.2.1).
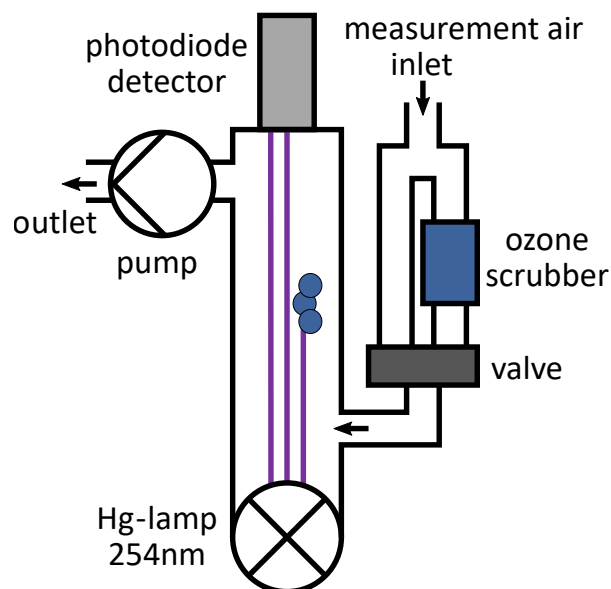

Figure 3:
A pump at the outlet provides a steady flow of measurement air through the absorption chamber. A mercury (Hg) lamp emits light at 254 nm (ultraviolet) in the direction of a photodiode detector for this wavelength. The intensity for unaltered air and air with the ozone removed by the ozone scrubber is measured. Comparing these two values, one gets the absorption caused by the ozone and thus can infer the ozone concentration.

Besides ozone, also some volatile organic carbon species, mercury vapor, aromatic photooxidation products and sulfur dioxide (SO_2) absorb at 245 nm. This leads to positive interference in the measurement of ozone concentration (Leston et al. 2005; Kleindienst et al. 1993). In volcanic plumes especially the high SO_2 concentrations pose an interference problem.
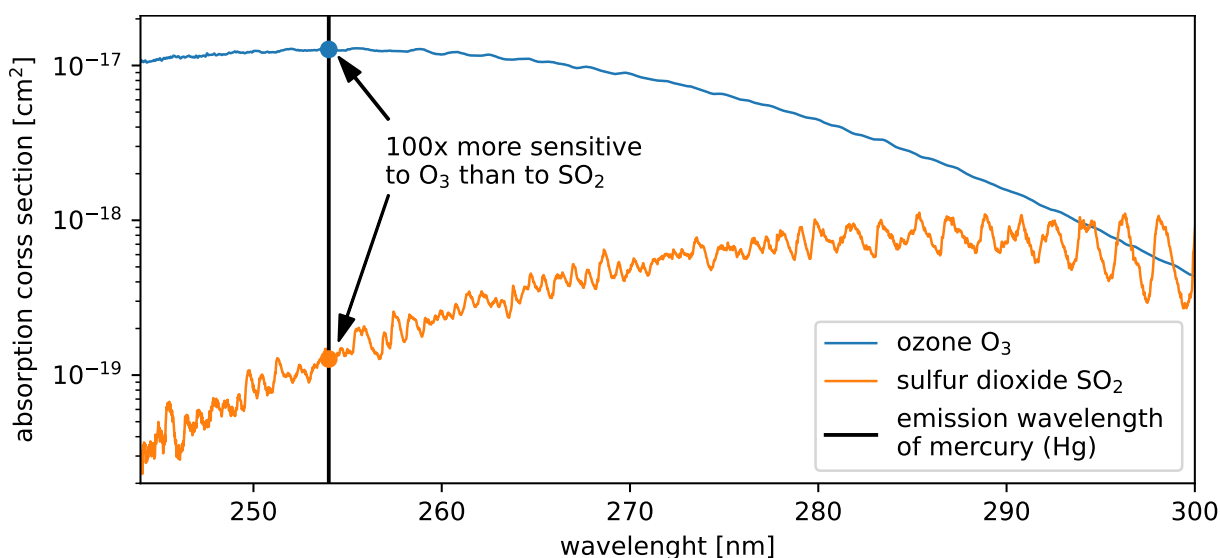

Figure 4: Absorption cross section of ozone and sulfur dioxide in the ultraviolet range. The vertical line marks the wavelength emitted by mercury lamps, that are used in UV absorption monitors. At this wavelength the cross section of ozone is 100 x larger than that of SO_2. (data from the HITRAN online data bank (Kochanov et al. 2019); O_3: (Birk and Wagner 2018); SO_2: (Hermans et al. 2009))

Figure 4 compares the absorption cross section of ozone and SO_2 in the UV range. At the wavelength used in UV absorption monitors the cross section of SO_2 is a factor 100 lower than that of ozone. This means that the UV absorption monitors are only 100 times more sensitive to ozone than to SO_2. Under normal atmospheric conditions there is less SO_2 than ozone, so the SO_2 concentrations induces an error less than 1% of the ozone measurement. Indeed, studies have shown that the interferences can be neglected under normal atmospheric conditions even with moderate pollution (Williams et al. 2006; Kleindienst et al. 1993). Therefore, UV absorption monitors are suited for air quality monitoring in urban and industrial areas.

However, this doesn't apply to measurements in volcanic plumes, because there SO_2 concentration can reach as high as several tens of ppm (Bobrowski et al. 2007), exceeding ozone by a factor of 1000. This causes an error ten times larger than the ozone signal (see table 2), compromising the ozone concentration measurements of UV absorption monitors in volcanic plumes.

	normal conditions	in volcanic plumes
typical ozone concentration	$\approx 40\,\mathrm{ppb}$	$\leq 40\,\mathrm{ppb}$
typical SO_2 concentration	$< 10\,\mathrm{ppb}$	up to $40\,\mathrm{ppm}$
absolute error induced by SO_2	$< 0.1\,\mathrm{ppb}\ O_3$	$400\,\mathrm{ppb}\ O_3$
relative error induced by SO_2	$< 1\,\%$	$1000\,\%$

Table 2: Overview of the situation in volcanic plumes and under normal conditions regarding ozone and SO_2 concentrations and the interference of SO_2 in ozone measurements with UV absorption monitors

Nevertheless, some of the studies in table 1 use these monitors and try to correct for the SO_2 interference. Surl et al. (2015) and Vance et al. (2010) use CrO_3 scrubbers to selectively filter out SO_2, but here humidity dependencies have to be considered. Kelly et al. (2013) and Rüth (2021) additionally measured SO_2 and corrected for the SO_2 impact in post processing calculations. But this leads to extremely high uncertainties because the SO_2 excess is so large.

We decided to bypass this problem by using the slightly more laborious measurement technique of ethylene chemiluminescence, that only suffers negligible interferences from other volcanic trace gases.

1.3 The First CL Ozone Monitor Prototype

The research group of Prof. Platt already uses a prototype based on the chemiluminescence of ozone with ethylene. It is based on the Bendix CL ozone monitor model 8002 from the 1980s. It was modified to reduce the weight and size and equipped with a digital data logger (for details see Rüth (2021) chapter 4.1). Now it weighs 10 kg and can be carried around by a person (see figure 5). It was used to conduct field measurements in a fumarole at Mount Etna in October 2020 (Rüth 2021, chapter 8). The problem is that the measurement opportunities in volcanic plumes for instruments carried by humans are very limited. The plume must be pushed to the ground in an area safely accessible to humans.

To overcome this problem, we are constructing a new, lightweight (target weight 1 kg) CL ozone monitor prototype that can be mounted on a drone. In this way, the instrument can take measurements in the plume at height altitude and at different distances from the crater.
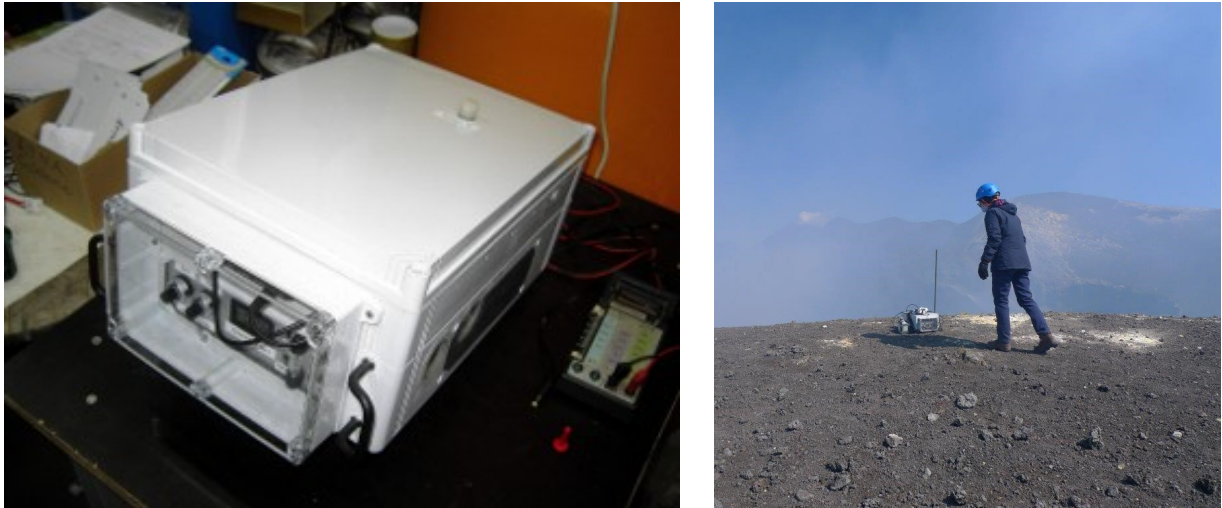

Figure 5: left: photo of the first CL ozone monitor in our working group; right: this monitor in action at Mount Etna

2 Theory of CL Ozone Monitor Operation

2.1 Measurement Principle and Chemistry

The ozone monitor constructed in this thesis uses the photon signal generated by the chemiluminescent reaction between ozone and ethylene, to draw conclusions about the ozone concentration. The principle is illustrated in figure 6.

With the help of a pump, a steady flow of measuring air through the reaction chamber is generated. There the air is mixed with ethylene (C_2H_4). The ozone in the air reacts with the ethylene in a fast, dry and flameless gas phase reaction that produces many different products. For more details on this reaction see Finlayson et al. (1974), Kleindienst et al. (1993), Rüth (2021, chapter 4.1.2) and references therein. Relevant here is the formation of excited formaldehyde ($HCHO^*$).

$$O_3 + C_2H_4 \longrightarrow HCHO^* + CH_2OO \tag{4}$$
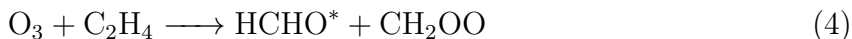
During the de-excitation ($^1A'' \rightarrow {}^1A_1$ transition), formaldehyde mainly fluoresces in the range from 400 to $480\,nm$ (see spectrum in figure 7). These photons are detected by a suitable photomultiplier tube (PMT) that is directly mounted on one side of the reaction chamber. The signal of the PMT can be linked to the ozone concentration by calibrations, during which air with a known ozone concentration is measured.
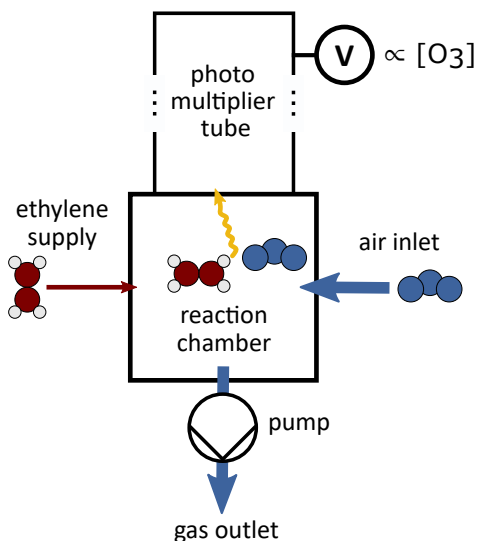

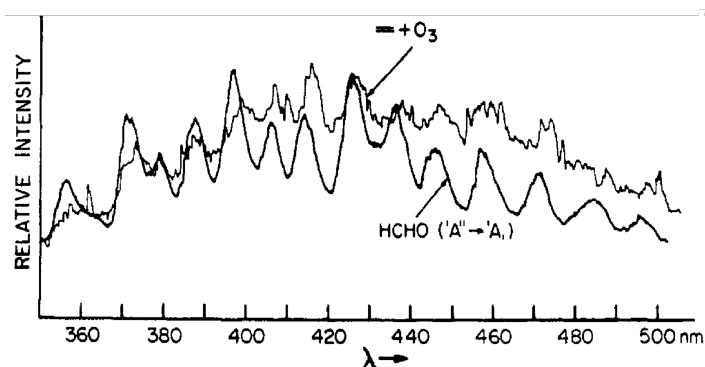**Figure 6:** Measurement principle of a ethylene chemiluminescence ozone monitor

Figure 7: Comparison of two spectra in the visible range; upper line O_3: chemiluminescent emission spectrum from the reaction of 2% O_3/O_2 with ethylene (C_2H_4), (at 4.5 Torr); lower line HCHO: formaldehyde fluorescence excited by tesla coil discharge ($^1A'' \rightarrow {}^1A_1$) (at 4.9 Torr)
source: Finlayson et al. (1974, figure 2 (i))

The signal of the PMT must be first-order dependent on the ozone concentration in order to make valid measurements. To establish these pseudo-first order conditions, ethylene must be provided in large excess. Thus, the ethylene concentration can be assumed to be constant over time.

2.2   Optimization of Ethylene and Total Flow Rate

In the following, the dependence of the photon signal on temperature T, pressure p, ethylene flow rate $f_{C_2H_4}$, total flow rate generated by the pump f_{tot} and volume V of the reaction cell is calculated. The reaction rate can be expressed by the following differential equation

$$\frac{d\,[O_3]\,(t)}{dt} = -k(T)\,[O_3]\,(t)\,[C_2H_4]$$

with $k(T)$ being the temperature dependent reaction constant given by Atkinson et al. (2006).

$$k(T) = 9.1 \cdot 10^{-15} \exp\left(-\frac{2580}{T}\right)$$

This can be solved to get the time dependent ozone concentration.

$$[O_3]\,(t) = [O_3]\,(t=0) \cdot \exp\left(-k(T) \cdot [C_2H_4]_0 \cdot t\right)$$

So, the fraction of ozone molecules that has reacted after time t is given by

$$R(t) = 1 - \exp\left(-k(T) \cdot [C_2H_4] \cdot t\right).$$

In the case of the ozone monitor a steady flow of air and thus ozone passes the reaction chamber. The fraction of reacted ozone in this flow is given by $R(t_{\text{flush}})$, because $R(t)$ can also be regarded as the probability of an ozone molecule having reacted after time t. The time t_{flush} is the mean residence time of an ozone molecule in the reaction chamber and is given by

$$t_{\text{flush}} = \frac{V}{f_{tot}}$$

with V being the volume of the reaction chamber.
From the ideal gas law the molecular density C in the reaction chamber can be derived.

$$C = \frac{\text{molecules}}{\text{volume}} = \frac{p}{k_B T}$$

The ethylene concentration is than simply given by

$$[C_2H_4] = \frac{f_{C_2H_4}}{f_{tot}} \cdot C$$

and for the ozone concentration the following relation holds

$$[O_3]: \quad 1\,\text{ppb} \mathrel{\hat=} 10^{-9} \cdot C.$$

Finally, this can be combined to an expression for the photons generated per second γ by the chemiluminescent reaction

$$\gamma = (f_{tot} - f_{C_2H_4})[O_3] \cdot R(t_{\text{flush}}) \cdot QE$$

$$= \frac{\text{volume}}{\text{time}} \cdot \frac{O_3 \text{ molecules}}{\text{volume}} \cdot \frac{\text{reactions}}{O_3 \text{ molecule}} \cdot \frac{\text{photons}}{\text{reaction}} = \frac{\text{photons}}{\text{time}}$$

10

Here $(f_{tot} - f_{C_2H_4})[O_3]$ is the number of ozone molecules that enter (and leave) the reaction chamber each second; $R(t_{\text{flush}})$ is the fraction of ozone molecules reacting and $QE \approx 10^{-7}$ is the quantum yield for the chemiluminescence (Kleindienst et al. 1993). The quantum yield is the probability that a reaction will lead to the emission of a photon, and it is so low since the excited formaldehyde can also lose its energy through collisions with other molecules, not only through the emission of a photon. The temperature and pressure dependence of the quantum yield is neglected in these calculations, as there is no detailed information on this in the literature.

The four graphs in Figure 8 show how the emitted photons per second γ and the fraction of the ozone molecules $R(t_{\text{flush}})$ that react with ethylene depend on four following parameters: the two ambient parameters temperature T and pressure p and the two instrument parameters ethylene flow $f_{C_2H_4}$ and total flow f_{tot}. While one of these four parameter is varied on the x-axis the others are held constant at realistic values. The number of emitted photons is proportional to the fraction of ozone molecules in the measurement air. In these graphs the calculations are done for an ozone mixing ration of 1 ppb.
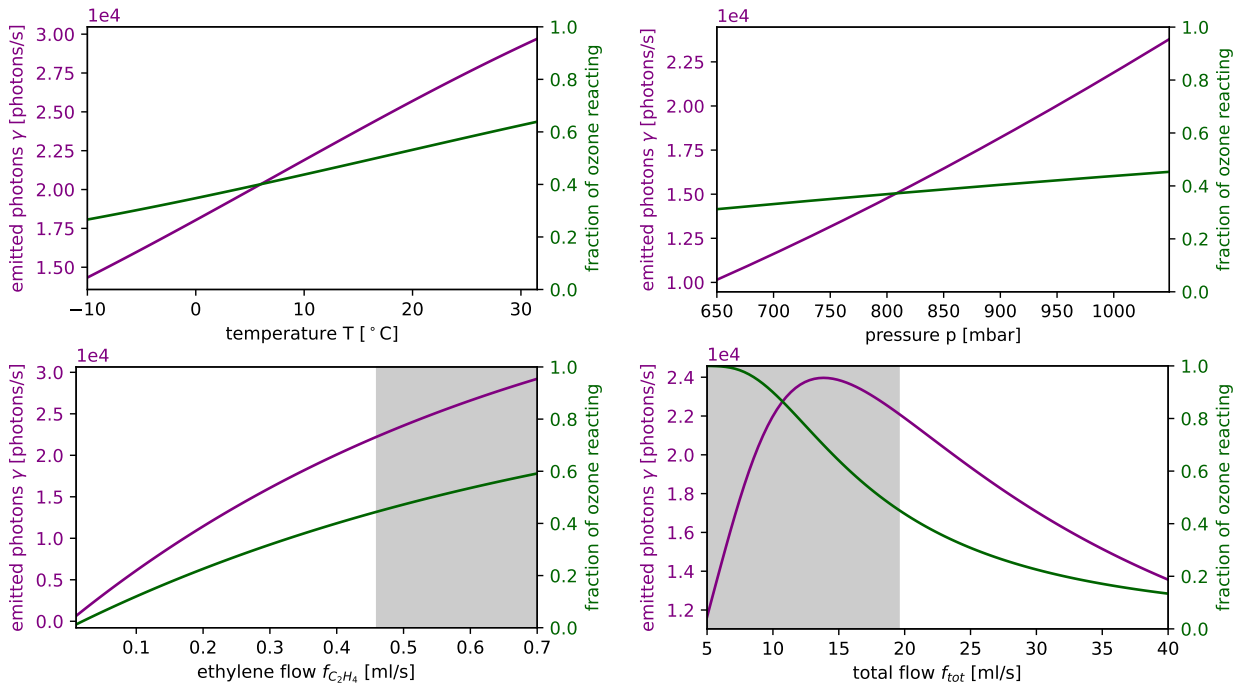

Figure 8: Dependency of the total number of generated photons per second γ (violet) and the fraction of ozone molecules that react with ethylene (green) on the ambient temperature T and pressure p as well as on the ethylene flow $f_{C_2H_4}$ and total flow f_{tot}. In every graph one parameter is varied while the others are held constant at $T = 10\,°C$, $p = 1\,bar$, $f_{C_2H_4} = 0.45\,ml/s$ and $f_{tot} = 20\,ml/s$ respectively (1 ppb ozone mixing ratio). The gray shaded areas are forbidden by the lower explosion limit for ethylene of 2.3 %.

In figure 8 the axis extend to quite low values of temperature and pressure, since the ozone monitor constructed in this thesis is to be used at high altitudes on Mount Etna (3357m). Higher temperature and pressure lead to an increase in the absolute photon signal (see upper graphs in figure 8) and to a decreased relative sensitivity to changes in

these ambient parameters. At $1\,\text{bar}$ and $10\,°\text{C}$ the photon signal changes by $390\,\frac{\text{photons}}{s\cdot\text{ppb}\cdot K}$, which corresponds to an increase of $1.8\,\%/K$ (at $-10\,°\text{C}$: $355\,\frac{\text{photons}}{s\cdot\text{ppb}\cdot K} \mathrel{\hat{=}} 2.5\%/K$; at $30\,°\text{C}$: $330\,\frac{\text{photons}}{s\cdot\text{ppb}\cdot K} \mathrel{\hat{=}} 1.1\%/K$). At $10\,°\text{C}$ and $1\,\text{bar}$ the pressure dependency is $38\,\frac{\text{photons}}{s\cdot\text{ppb}\cdot\text{mbar}}$, corresponding to a rise of $0.17\,\%/\text{mbar}$ (at $700\,\text{mbar}$: $30\,\frac{\text{photons}}{s\cdot\text{ppb}\cdot\text{mbar}} \mathrel{\hat{=}} 0.26\,\%/\text{mbar}$).
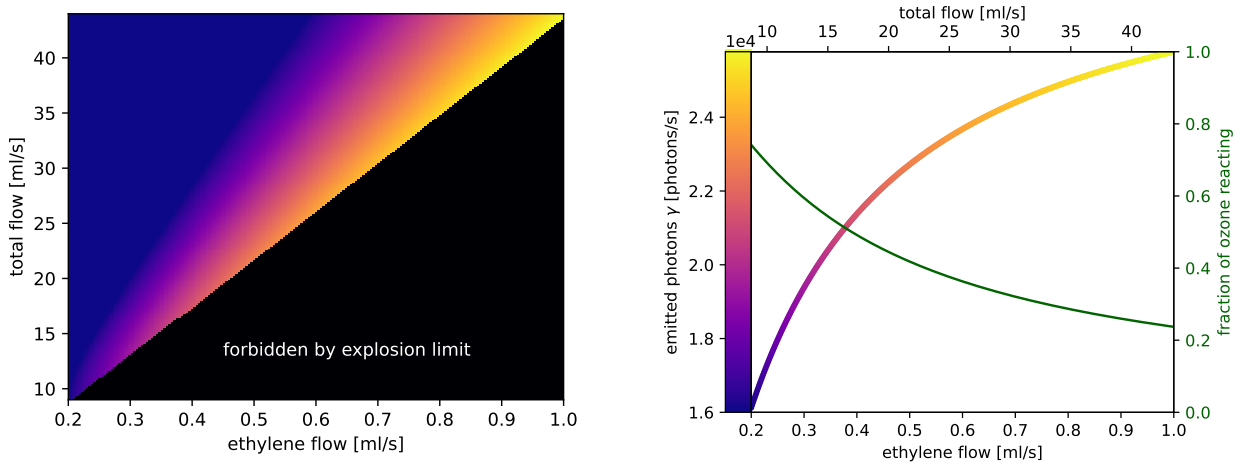

Figure 9: The colour map shows the dependency of the total number of photons generated per second on the ethylene flow $f_{\text{C}_2\text{H}_4}$ and the total flow f_{tot} through the reaction chamber. The highest values are directly on the diagonal border to the area forbidden by the explosion limit for ethylene of $2.3\,\%$. The right graph depicts the emitted photons and the fraction of ozone reacting along this diagonal with $f_{\text{C}_2\text{H}_4} = 0.023 \cdot f_{tot}$. At temperature $T = 10\,°\text{C}$, pressure $p = 1\,\text{bar}$, ozone concentration $[\text{O}_3] = 1\,\text{ppb}$

The ethylene flow $f_{\text{C}_2\text{H}_4}$, the total flow f_{tot} and the volume V of the reaction cell are adjustable system parameters. The aim is to maximize the photon signal, while maintaining the boundary conditions. These are the explosion limit for ethylene in air $f_{\text{C}_2\text{H}_4}/f_{tot} \leq 0.023$, the response time of the device (t_{flush} should be rather small) and that the size and the weight of the reaction chamber and ethylene supply are limited, since the monitor must be carried by a drone.

The volume of the reaction chamber is fixed at $20\,\text{ml}$ (see section 2.3). The colour chart in Figure 9 shows the number of emitted photons for the different combinations of ethylene flow and total flow. The black area is prohibited by the explosion limit, because the ethylene concentration would be higher than $2.3\,\%$. The highest photon signal in each row and column is directly at the border of the forbidden area, so that one should maximise the permissible ethylene concentration. The lower graphs in figure 8 show the variation of one row and one column respectively. Larger flow rates give shorter response time and higher photon emissions, when keeping the ratio between ethylene and total flow constant at 0.023 (diagonal in the colour chart; Figure 9 right). The ethylene consumption and the size of the ethylene storage container set a limit to the flow rates selected. We chose preliminarily $f_{\text{C}_2\text{H}_4} = 0.45\,\text{ml}\,\text{s}^{-1}$ and $f_{tot} = 20\,\text{ml}\,\text{s}^{-1}$, but this can still be adjusted relatively easily.

2.3   Optimization of Reaction Chamber Volume

It is an interesting question how many of the chemiluminescent photons actually reach the sensitive area of the photomultiplier tube (PMT). Therefore, a simple simulation (s. Figure 10 left) calculates the trajectory of a large number of photons. It is assumed that the circular photosensitive area of the detector (the photocathode of the PMT) covers one end of the cylinder (green circle). So the radius R of the reaction chamber is determined by the chosen PMT (here: $R = 14.25\,\text{mm}$). The length L is varied. For each length 100000 photons are generated randomly. They are uniformly distributed within the cylinder volume. The emission direction is chosen randomly with a uniform distribution as well. When a photon hits the reaction chamber wall (side or back wall) it is either absorbed or reflected diffusely (reflectivity ρ). The new direction is chosen randomly following Lambert's cosine law. The simulation counts how many of the photons reach the photosensitive area in less than 50 reflections. This leads to an underestimation for large reaction chambers and high reflectivity. But even for reflectivity $\rho = 0.96$ and $L/2R > 2$ the fraction of photons that are neither absorbed nor detected after 50 reflections is less than $0.3\,\%$.
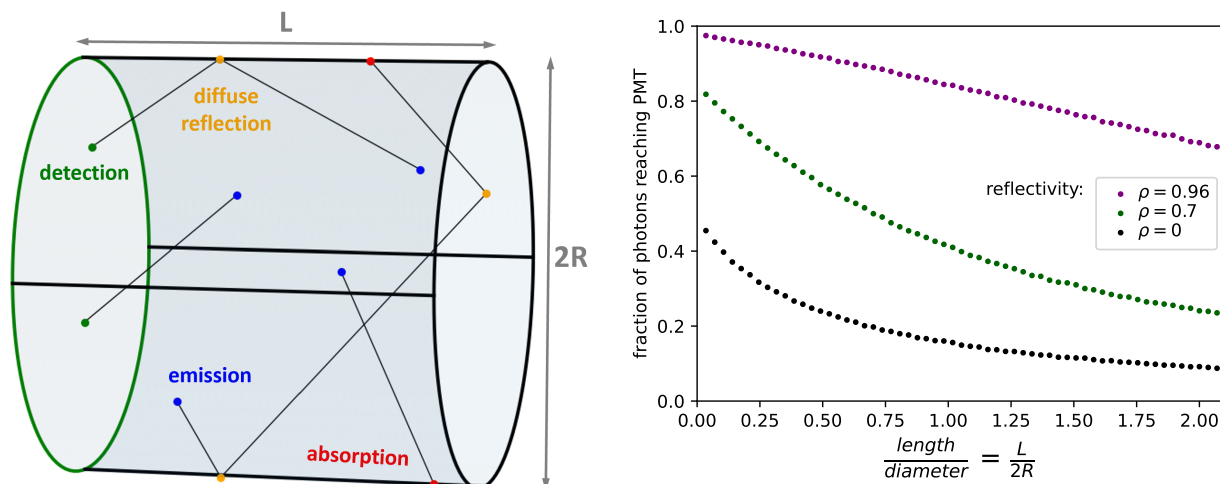

Figure 10: *left:* Model of the cylindrical reaction chamber with some photon trajectories, the left side (green) is the photosensitive area of the PMT.
right: Fraction of photons reaching the photosensitive area as a function of the reaction chamber dimensions for different reflection indices of the walls.

Figure 10 (right) shows the result of the simulation for three different reflection indices $\rho = 0$, 0.7 and 0.96. The case with zero reflectivity $\rho = 0$ (or 100% absorptivity) illustrates the proportion of photons that reach the detection area directly and without reflections. The fraction reaching the PMT decreases for more elongated reaction chambers, since the ratio between photosensitive area to wall area is smaller. But a higher reflectivity of the walls can counteract this, because then the photons are on average more often reflected and have more opportunities to reach the PMT before being absorbed.
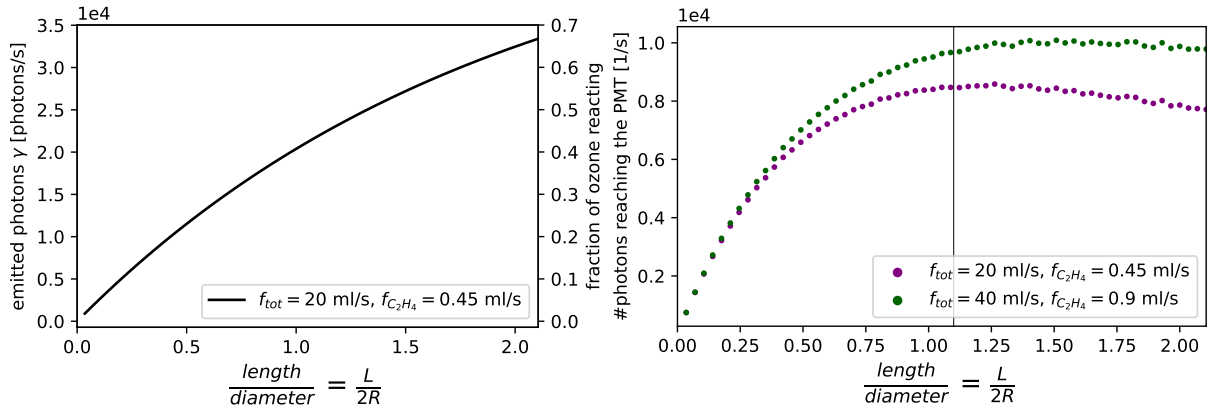
Figure 11: As a function of the ratio between length and diameter of the reaction chamber:

left: total number of emitted photons per second and the fraction of ozone molecules that react with ethylene (analog to the graphs in figure 8)

right: Number of photons reaching the PMT for two different sets of flow rates with reflectivity $\rho = 0.7$. Calculated by multiplying the values from the left graph with those from figure 10 (right). Marked by the vertical line is the chosen value of $L = 31.35\,\text{mm}$

parameters: temperature $T = 10\,°\text{C}$, pressure $p = 1\,\text{bar}$, ozone concentration $[O_3] = 1\,\text{ppb}$

The goal is to optimise the length of the reaction chamber to maximise the total number of photons reaching the PMT. The volume of the reaction chamber and thus its length also has an influence on the total number of photons emitted. If the reaction chamber is larger, a larger proportion of the ozone molecules will react because the mean residence time t_{flush} is greater (see figure 11 left). Multiplying the fraction of photons reaching the PMT with the total number of photons emitted yields the number of photons reaching the PMT (see figure 11 right). We chose $L = 31.35\,\text{mm}$ as the length of the reaction chamber. With the Radius $R = 14.25\,\text{mm}$ (= radius of the sensitive area of the PMT) the reaction chamber has a volume of $V = \pi R^2 L = 20\,\text{ml}$ and a ratio of $\frac{L}{2R} = 1.1$. For the chosen values $f_{\text{C}_2\text{H}_4} = 0.45\,\text{ml}\,\text{s}^{-1}$ and $f_{tot} = 20\,\text{ml}\,\text{s}^{-1}$, about 8400 photons/s reach the PMT for $1\,\text{ppb}$ of ozone according to figure 11 (right), which corresponds to only $13\,\frac{\text{photons}}{s\cdot\text{mm}^2}$.

Lengthening the reaction chamber would not lead to a substantial increase of incident photons. Figure 11 even predicts an decrease of incident photons for greater length, but this is probably caused by too much simplification of the model. The simulation assumes that the photons are emitted evenly distributed across the reaction chamber. In reality the concentration of ethylene and ozone are not homogeneous in the reaction chamber and more reactions occur close to the inlets of measurement air and ethylene. Therefore, these inlets should be positioned close to the PMT.

The reaction chamber of the new prototype is made of unpolished aluminum and we estimate its reflectivity to $\rho = 0.7$. For the chosen dimensions a doubling of the flow rates (figure 11 left) leads only to an increase of 14% of the number of photons reaching the PMT. Increasing the reflectivity of the walls can have a much greater impact. Therefore, we plan to make a second reaction chamber with an inner layer of ODM98 (Gigahertz Optik GmbH 2022), that has a reflectivity of over $\rho = 0.96$ at the relevant wavelength.

Figure 10 (right) shows that this would more than double the number of incident photons. With such a high reflectivity, an increase in the size of the reaction chamber would also lead to a further increase in incoming photons. However, the realization of this improved reaction chamber is not part of this thesis.

3 Realization of the New Lightweight Prototype

Figure 12 shows a schematic drawing of the new prototype, the components of which are shown in figure 13. The working principle is explained in chapter 2.1. The following chapters will explain the components of the new prototype in detail, referring to the labels in figure 13. The appendix 7.3 contains a list of the relevant data sheets.

The instrument, as shown in figure 13, weighs 1100 g, but some components and the housing are still missing.
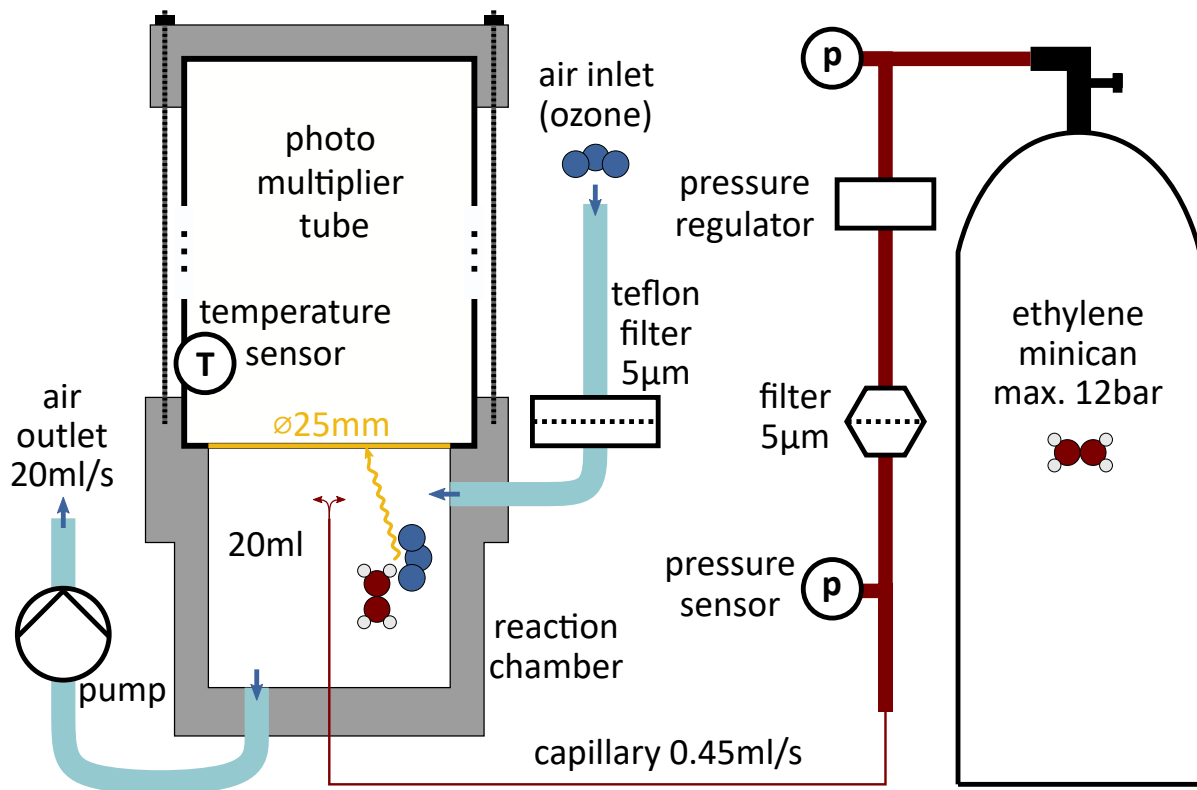

Figure 12: Schematic drawing of the new chemiluminescence ozone monitor prototype setup (without the electronics); compare to the measurement principle in figure 6 and the photo of the setup in figure 13
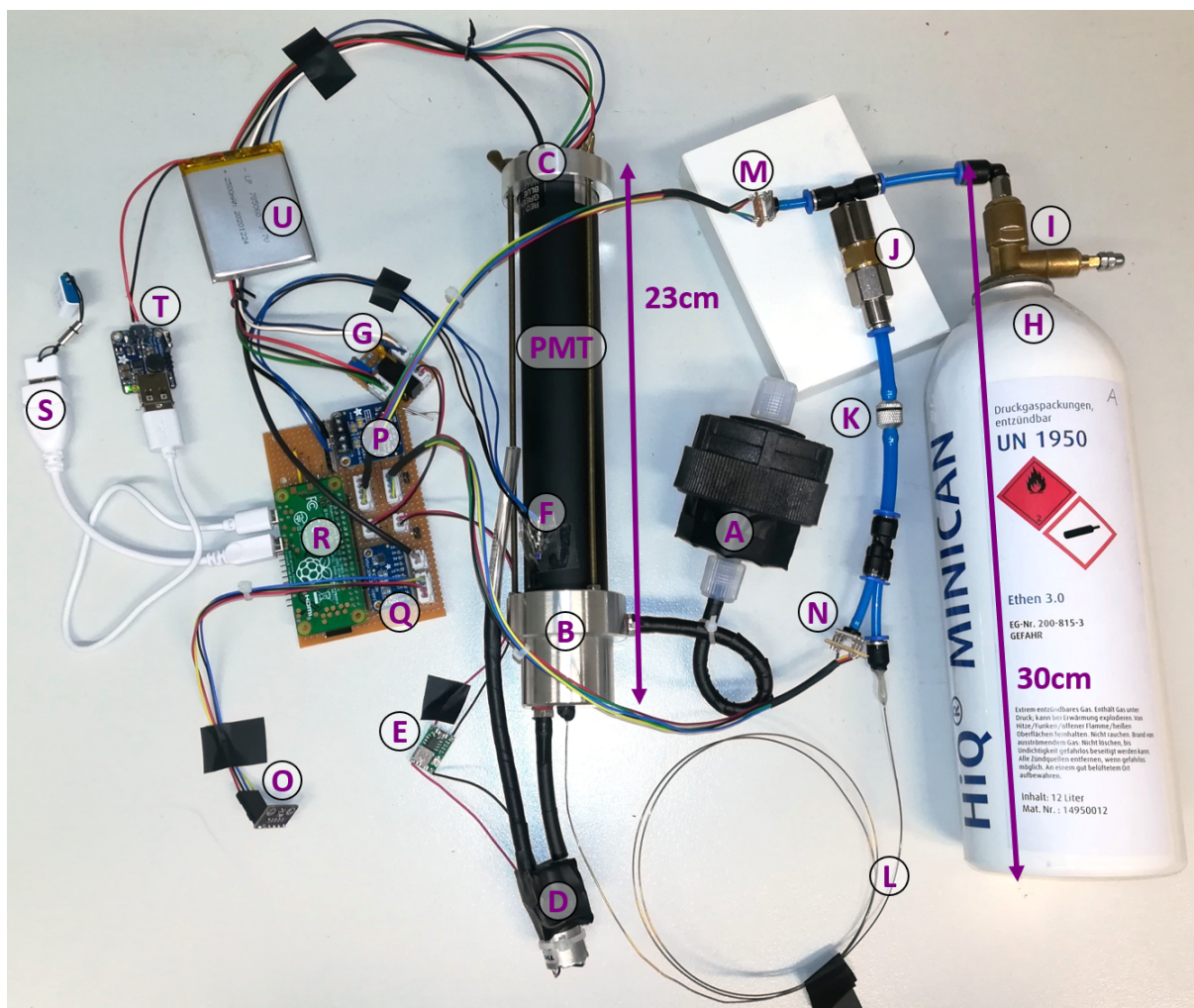
Figure 13: Photo of the new chemiluminescence ozone monitor prototype. See the text for detailed description of the parts

A	inlet filter	**K**	filter
B	reaction chamber	**L**	capillary
C	fixing clamp	**M**	pressure sensor for minican
D	pump	**N**	pressure sensor for capillary
E	voltage converter for pump	**O**	ambient sensor (temperature, pressure)
PMT	photomultiplier module	**P**	analog-to-digital converter for PT1000
F	PT1000 temperature sensor	**Q**	analog-to-digital convertor for PMT
G	supply board for PMT	**R**	Rasperry Pi Zero computer
H	ethylene bottle (minican)	**S**	USB Stick
I	manual valve	**T**	booster for power supply
J	mini pressure regulator	**U**	lithium-polymer battery

3.1 Air Flow Control (A-E)

A PTFE Filter

A sample gas filter with 5 µm pore size at the inlet prevents aerosols from entering the instrument. It is made from PTFE (Teflon) with glass fiber supporting fabric. The new prototype uses the same filters as the old one (remark: the filters are white, but in the storage box they are separated by light blue paper discs; don't confuse them). The filter holder and hose (4 mm ID (inner diameter), 6 mm OD (outer diameter)) are also made out of Teflon. As ozone is very reactive, everything that comes into contact with the measuring air before it enters the reaction chamber must be made of an inert material (such as Teflon). Otherwise, the destruction of ozone on the way to the reaction chamber would affect the measurements. The hose is bend around itself and everything is covered with black tape to prevent photons from entering the reaction chamber. The hose is linked to the reaction chamber by a hose connector with M5 external thread.

B Reaction Chamber

The reaction chamber is made out of aluminium and was crafted in the institute's workshop according to our technical drawing. It is cylindrical with one end covered by the photosensitive area of the PMT and has a volume of 20 ml (inside: length 31.35 mm, diameter 28.5 mm). The choice of dimensions of the reaction chamber are discussed in chapter 2.3. The layout of the inlets and outlet was changed in comparison to the old prototype (see figure 14). The ethylene flow is much smaller than the measurement air flow, so most of the reactions take place near the the ethylene inlet. Consequently, we want the point where the ethylene enters the reaction chamber to be close to and centered in front of the photosensitive area of the PMT. Therefore, we decided to have the capillary extend from the centre back to the front of the reaction chamber. The air inlet and the gas outlet do not extend into the reaction chamber. This arrangement obscures the sensitive area as little as possible. The air inlet is on the side wall near the PMT and the gas outlet is on the opposite side on the rear wall. This maximises the path of the gas molecules through the reaction chamber and leaves as little 'dead space' as possible. To save weight, the walls of the reaction chamber are just thick enough to accommodate the necessary screw threads. The PMT is attached to the reaction chamber by clamping it between two metal parts (**B** and **C**) and building up a small amount of pressure with three long screw threads.
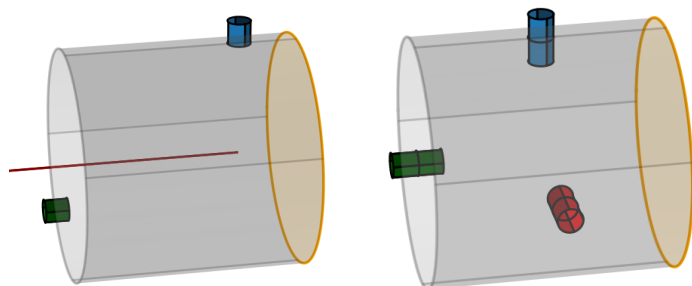

Figure 14:
Layout of the reaction chamber of the new prototype (left) and the old prototype (right)
red: ethylene inlet (capillary)
blue: air inlet
green: gas outlet
orange: photosensitive area (PMT)

D The Pump

We use a rotary vane pump of the model G 6/01-K-LC (Thomas by Gardner Denver) to generate the air flow. It is attached to the gas outlet of the reaction chamber (see fig 14) by a hose connector (same as on the inlet, M5 external thread) and a rubber hose (4 mm ID, 6 mm OD). Another hose leads to the exhaust. Here too, as at the entrance, everything is wrapped in black tape to prevent photons from entering the reaction chamber.

According to the data sheet, the pump has a maximal flow rate of $2.2\,l\,min^{-1}$ at 6 V DC. By applying a lower voltage one can control the flow rate. The relation was measured in our lab and is shown in figure 15. An adjustable mini step-down converter (**E**, from sertronics, ordered at Berrybase article nr.: REGA3A) is connected between the pump and the overall power supply. It takes an input voltage and ground and converts it to a lower output voltage and ground. The output voltage can be set with a potentiometer. For an input voltage of 5.0 V the adjustable range is 0.5 V to 4.8 V.
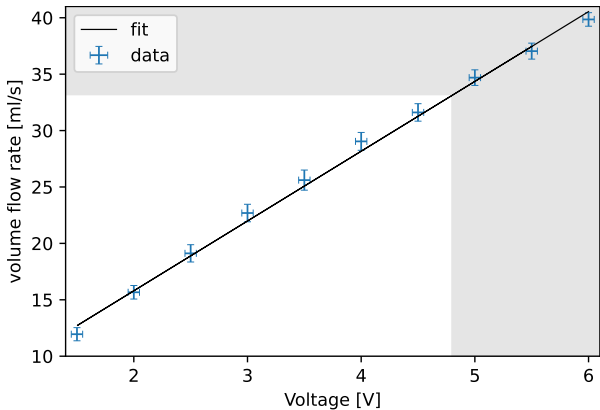

Figure 15:
Volume flow rate of the rotary vane pump as a function of the applied voltage. The voltage comes from a laboratory power supply and the flow was measured with a thermal mass flow meter (Model 4140 from TSI). The grey shaded area is not accessible because of the limited range of the voltage regulator (**E**) used in the instrument. A linear fit $y(x) = a \cdot x + b$ has the results $a = 6.19 \pm 0.13$ ml s^{-1} V^{-1} and $b = 3.4 \pm 0.5$ ml s^{-1}.

3.2 Photomultiplier Module (PMT-G)

Nowadays, there are several ways to detect light, including photomultiplier tubes (PMT), photodiodes, avalanche photodiodes and silicon photomultipliers. Chemiluminescence produces diffuse light, so a large light-sensitive area is needed. At the same time, despite the large area, the noise and dark current must be small enough that it does not exceed the signal. Also, the calculations in chapter 2.3 showed that one can expect only about $13\,\frac{photons}{s\cdot mm^2}$ reaching the front area of the cylindrical reaction chamber. With this extremely low diffuse light incidence, a PMT is the only sensible choice (Hergert and Piatek 2017, in particular see figure 8).

In contrast to the old prototype, we decided to omit cooling the PMT in order to reduce weight and energy consumption. In order to provide a basis for this decision a series of 14 experiments was performed during several month in the summer 2021. The dark current of the photomultiplier tube of the old prototype was measured over a wide temperature range, while its cooling was turned off. This dataset is shown in figure 16 and consists of more than 1 million data points summing up to over 270 h of measurement time. The

temperature was measured with a BME280 (from adafruit) that is positioned close to the reaction chamber. The dark current signal is given in ozone mixing ratio equivalents. But no ozone was measured during these experiments, as an ozone scrubber was attached to the inlet and no ethylene was added.
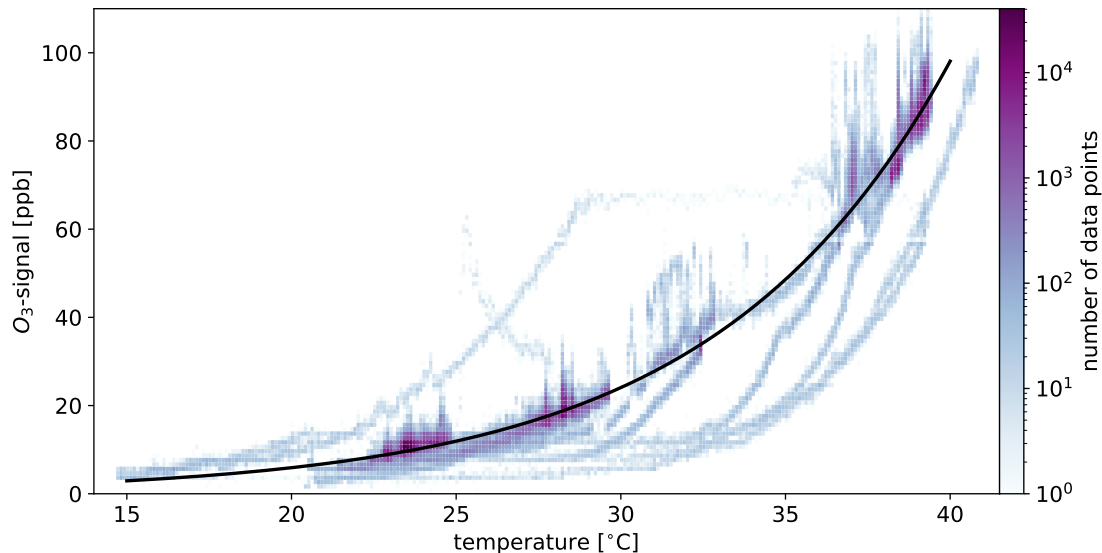

Figure 16: The dark current signal of the photomultiplier tube of the old prototype as a function of the temperature. The colour indicates how many data points have the same temperature dark signal relation. An exponential fit $I(T) = I_0 \cdot e^{T/\Theta}$ yields $\Theta = 7\,\mathrm{K}$ and $I_0 = 0.36\,\mathrm{ppb}$ (black line).

While the majority of data points lie on an exponential curve, there are also some deviating branches (see figure **??**fig:darkcurrent). These originate from experiments, during which the ambient temperature was changed rapidly. In the other experiments the temperature was relatively constant over many hours. The deviations are caused by the temperature sensor adapting to the ambient temperature faster than the photocathode in its tube with a large heat capacity. The measured temperature therefore does not match the temperature at the photocathode, which determines the size of the dark current. However, if one can ensure that really the temperature of the PMT is measured, the size of the dark current signal can be predicted well.

For this purpose, a small PT1000 temperature sensor (temperature dependent platinum resistor) is installed directly on the surface of the new PMT (**F**). Due to its small size and thus its low heat capacity, it always has the same temperature as the PMT. In addition, a piece of well-insulating material (styrofoam) can be glued on top of the PT1000 to isolate it from the environment. Furthermore, one can determine the background signal at each measurement by using ozone scrubbers.

From the exponential fit in figure 16 one can calculate that the dark current increases tenfold for a 16 K temperature rise.

$$\text{fit parameter: } \Theta = 7\,\text{K} \quad \rightarrow \quad \Theta_{10} = \ln 10 \cdot \Theta = 16\,\text{K}$$

This agrees well with Richardson's law, which predicts a tenfold increase for a 15 °C temperature rise for the typical bialkali cathode used in the old prototype (photonis n.d. page 16). In this temperature range, thermionic emission is responsible for the dark current, which mainly depends on the material of the cathode. So these results can be transferred to the new photomultiplier, as it has a cathode made of the same material in order to be sensitive in the correct wavelength range (see figure 7). Nevertheless, the temperature dependency of the new PMT should be determined separately.

Finally, we decided to use the Photosensor Module H10493-001 from Hamamatsu Photonics GmbH. The included 28.5 mm diameter head-on (front-window) photomultiplier tube has a large effective area of at least 25 mm diameter ($490\,\text{mm}^2$). Like the PMT from the old prototype, it has a bialkali cathode, that has the required spectral response from 300 nm to 600 nm with a peak sensitivity wavelength of 420 nm. It is a module, that already incorporates the high voltage power supply and a low noise amplifier. This makes it really easy to use. A coaxial cable carries the voltage output signal, which is read out by an analog-digital-converter (**Q**). The photomultiplier module only requires an input voltage of ± 11.5 V to ± 15.5 V for power supply. Also, a control voltage between +0.5 V and +1.4 V has to be supplied to adjust the gain (i.e. the high voltage) of the PMT. This can be done with a 10 kΩ potentiometer dividing the provided reference voltage of 2.5 V. Therefore, 5 wires lead to the PMT supply board (**G**) shown in figure 17 (see also the circuit diagram in the appendix 7.1). This board holds the voltage divider as well as a DC/DC-converter which takes the +5 V overall power supply and provides ±15 V.
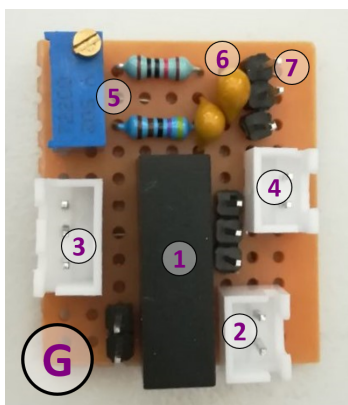

Figure 17: Supply board for the photomultiplier (**G**):

1. DC/DC-converter from 5 V/DC to ±15 V/DC (TracoPower TMA 0515D)
2. connector to the overall power supply (+5 V and GND)
3. connector to the PMT (±15 V and GND)
4. connector to the PMT (reference and control voltage)
5. voltage divider (top: 10 kΩ, left: 5.22 kΩ potentiometer, bottom: 4.7 kΩ)
6. capacitors (10 µF) to smooth out the control voltage

The board as it is shown in figure 17 causes two problems at the moment and has to be revised. Firstly, with a stable 5 V overall power supply the voltage provided by the DC/DC-converter is too high (± 16 to 17 V), so the converter should be exchanged by one providing ±12 V. Secondly, the reference voltage drops, when it is applied to the voltage divider, so the upper range of the control voltage is not accessible. Therefore, the resistor values in the voltage divider have to be adjusted.
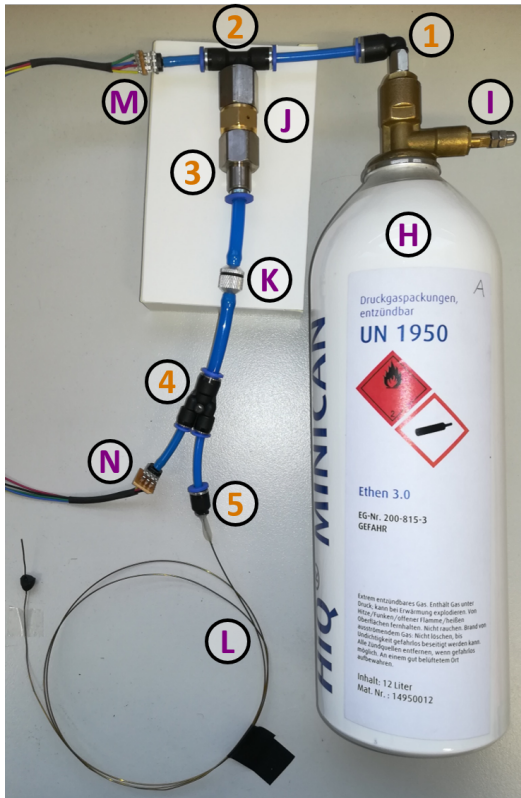
3.3 Ethylene Supply (H-O)

Figure 18: Ethylene supply

H	ethylene minican
I	manual valve
J	pressure regulator
K	filter
L	capillary
M, N	pressure sensors
1 - 5	adapters

Figure 19: Experimental setup for measuring the ethylene flow: The measuring cylinder is filled to the top with water at the beginning. The ethylene flows out of the capillary and is collected in the measuring cylinder with the help of a pneumatic trough. The experimenter stops the time until a certain volume of water is displaced by the gas. Dividing the replaced volume by the stopped time gives the ethylene flow.

H Ethylene Minican

The ethylene gas is stored in a small pressure bottle (minican) that can be refilled from a larger gas tank. It has a volume of $1\,\mathrm{L}$ and a maximum overpressure of $12\,\mathrm{bar}$ (overpressure = pressure relative to the atmosphere (differential)). This corresponds to $12\,\mathrm{L}$ of ethylene gas at atmospheric pressure. But the bottle must not be emptied completely, because the pressure regulator needs a certain overpressure and backflow must be prevented. That means about $8\,\mathrm{L}$ are available for the instrument. At an ethylene flow of $0.45\,\mathrm{ml\,s^{-1}}$, this is sufficient for about $5\,\mathrm{h}$ of operation. Airborne measurements will take less time due to the limited battery capacity of the drone and the minicans can be easily exchanged between flights.

The ethylene minican is connected to a valve (**I**) that has to be opened and closed manually with a hexagonal screwdriver. The new prototype uses the same minicans and valve as the old prototype. The pressure in the minican and thus its gas level is monitored by a digital pressure sensor (**M**).
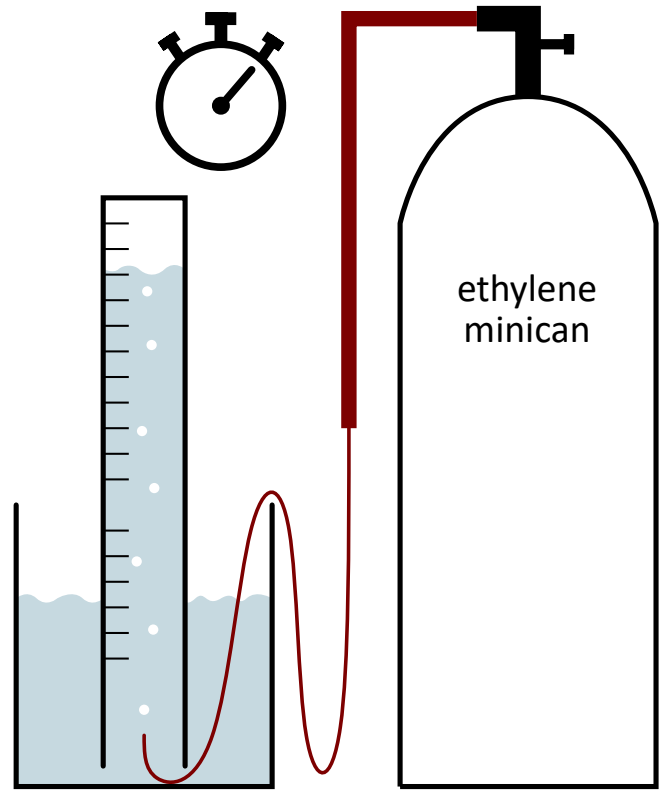
J   Pressure Regulator

The pressure in the minican varies depending on the filling level, but the ethylene flow should be constant over time. So the pressure has to be lowered to an appropriate steady value by a pressure regulator. The model (type nr. 638.42, bought from filcom and HUG-technik) used in the new prototype has a preset working pressure of 2 bar and does not have secondary venting. It has a G1/4" outer thread on both sides. This pressure regulator is very small and light (14 g), but it does not provide stable pressure, as the measurement in figure 20 shows. While the pressure in the minican decreases linearly over time because it is emptied (green curve), the pressure after the pressure regulator also decreases (violet curve), while it should actually remain constant. The decrease is very steep at the beginning after opening the valve and then reduces steadily over time. However, the pressure does not stabilise completely even after over an hour.
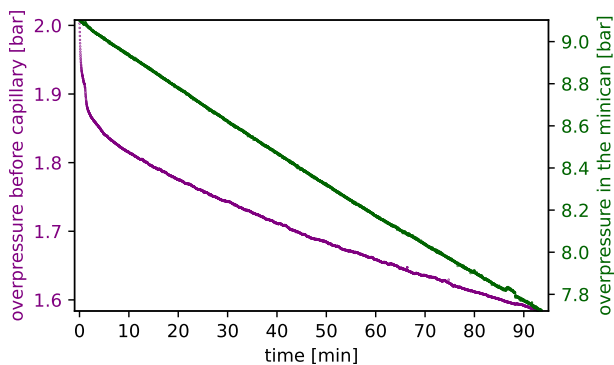

Figure 20: Temporal evolution of the overpressure before (green, right scale) an after (violet, left scale) the pressure regulator. The former is the pressure in the minican and was measured by pressure sensor **M**. The latter is the pressure before the capillary and was measured by pressure sensor **N**. The valve of the minican is opened at the start.

We tried to increase the pressure again by tapping on the pressure regulator to loosen its membrane. This can cause the pressure to rise again, but is not really predictable and leads again to rapid changes, as can be seen in figure 21.
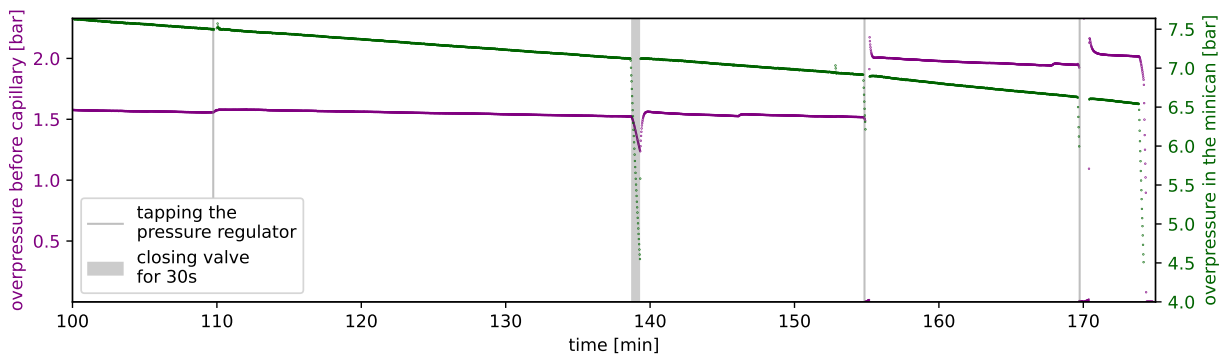

Figure 21: Reactions of the pressure levels in the ethylene supply line on tapping the pressure regulator or closing the valve for a few seconds

The pressure supplied by the pressure regulator does not depend on the absolute value of the pressure in the bottle, but on the decrease in pressure since the valve was opened (see figure 22). If you close the valve, let the pressure in the supply line equalise, and then put everything back together, the pressure from the pressure regulator will be high again. However, the starting value after opening the valve is not always the same and there is no clear relationship for the pressure provided by the pressure regulator.

22

There are two ways to solve this problem. One could use a better pressure regulator, but that would probably mean considerably more weight and higher costs. Or one could compensate for the fluctuations during post-processing. To do this, the ethylene flow would have to be closely monitored. But it is not really possible to install a flow meter in the feed line, and the method shown in Figure 19 is not applicable during operation. However, the pressure upstream of the capillary has a clear linear relationship to the flow rate and can be monitored very well with the second digital pressure sensor (**N**). One can perform calibration measurements with drifting pressures before the capillary to determine the direct correlation between pressure changes and ozone signal.
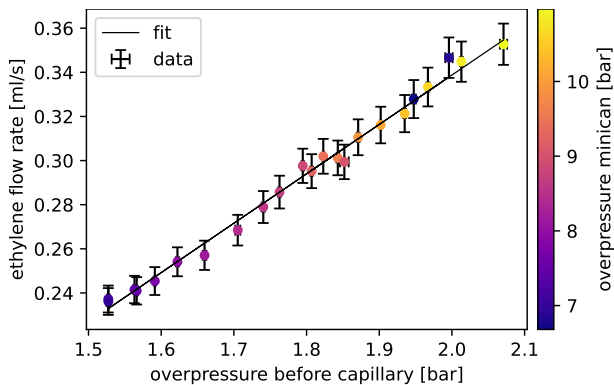

Figure 22: Ethylene flow rate as a function of the overpressure before the capillary (measured by pressure sensor **N**). Additionally the simultaneous overpressure in the minican is indicated by the color (measured with pressure sensor **M**). The flow rate was determined by the method explained in figure 19. A linear fit $f(p) = ap + b$ gave $a = 0.224 \pm 0.004 \ \mathrm{ml\,s^{-1}\,bar^{-1}}$ and $b = -0.109 \pm 0.008 \ \mathrm{ml\,s^{-1}}$.
length of the capillary: $1\,\mathrm{m}$

L   The Capillary

A capillary at the end of the supply line limits the flow of ethylene. We use a metal capillary with an outer diameter (OD) of $0.65\,\mathrm{mm}$ and an inner diameter (ID) of $0.15\,\mathrm{mm}$ (radius $r = 0.075\,\mathrm{mm}$). Because of this small diameter particles could easily clog the capillary. Therefore, a filter (**K**) is inserted upstream. It uses the same filter membranes as the filter at the inlet (**A**), cut to the required size.

The Hagen-Poiseuille equation describes the relation between the pressure difference Δp between the ends of the capillary and the flow f.

$$f = \frac{dV}{dt} = \frac{\pi \, r^4 \, \Delta p}{8 \, \eta \, l}$$

The dynamic viscosity of ethylene (at $10\,°\mathrm{C}$, $1\,\mathrm{bar}$) is $\eta = 9.8 \cdot 10^{-6}\,\mathrm{Pa\,s}$ (Engineering ToolBox 2018). By rearranging the equation, we find that theoretically the capillary has to be $48\,\mathrm{cm}$ long in order to obtain a flow of $f = 0.45\,\mathrm{ml\,s^{-1}}$ at a pressure difference of $\Delta p = 1.7\,\mathrm{bar}$. However, the manufacturer information about the diameter is not exact and the equation is extremely dependent on the diameter, because it enters to the 4th power. So we have no choice but to find the right length for the capillary by successive shortening and testing. The capillary installed in the new prototype at the moment is $1\,\mathrm{m}$ long. The ethylene flow is considerably smaller than $0.45\,\mathrm{ml\,s^{-1}}$ (see figure 22) so the length still needs to be adjusted.

1-5 Hose Adapters

To connect the functional parts of the ethylene supply line adapters and hoses are needed (see figure 18). The hoses adjacent to the filter (**K**) have 4 mm ID and 6 mm OD. All other blue hoses have 2 mm ID and 4 mm OD. They must be rigid enough to seal against up to 12 bar overpressure with push-in connectors.

Adapters as labeled in figure 18:

1 This rotatable L-shaped adapter connects to the valve with a M5 outer thread. On the other side it has a push-in connector for a hose with 4 mm OD. This push-in connector is used to easily disconnect the ethylene minican from the instrument. ('Blaue Serie' type nr. 125.005-4 from HUG-technik)

2 This T-shaped adapter has two ends to connect to 4 mm OD hoses and one end with a G1/4 inch inner thread that connects to the pressure regulator. (nr. 0101073006)

3 This linear adapter converts from a G1/4 inch inner thread (for the pressure regulator) to a hose with 6 mm OD. (nr. 0101008006)

4 This Y-shaped adapter splits from a 6 mm OD to two 4 mm OD push-in connector. (nr. 0102112004)

5 A small hole was drilled into a 4 mm OD plug-in cap to fit the capillary with a hot glue gun. (nr. 0101162002)

Adapters **2-5** are from Samaco GmbH.

3.4 Electronics and Sensors (M-U)

M-N Pressure Sensors

Two basic amplified board mount pressure sensors from Honeywell (ABP series, bought at RS components GmbH) monitor the pressure in the ethylene supply line. Their output indicates the difference between applied pressure and ambient pressure (Gage). The upper sensor **M** (nr. ABPDANV150PGSA3) measures the pressure in the ethylene minican and thus indicates the fill level. It has a range from $p_{min} = 0$ to $p_{max} = 150\,\mathrm{psi} \approx 10.34\,\mathrm{bar}$. The lower sensor **N** (nr. ABPDANV030PGSA3) monitors the pressure in front of the capillary, which is provided by the pressure regulator. The measured pressure is equivalent to the pressure difference between the two ends of the capillary, because there is ambient pressure in the reaction chamber. It has a range from $p_{min} = 0$ to $p_{max} = 30\,\mathrm{psi} \approx 2.07\,\mathrm{bar}$.

Both sensors incorporate an analog-to-digital-converter. Their output is a 14-bit number that can be read out via the Serial Peripheral Interface (SPI). The output number N is related to the applied pressure p by

$$N = 2^{14} \cdot \left(\frac{0.8}{p_{max} - p_{min}} (p - p_{min}) + 0.1 \right) = 2^{14} \cdot \left(\frac{0.8}{p_{max}} \, p + 0.1 \right)$$

One can count back from the output to the measured pressure by

$$p = (N \cdot 2^{-14} - 0.1) \frac{p_{max} - p_{min}}{0.8} + p_{min} = (N \cdot 2^{-14} - 0.1) \frac{p_{max}}{0.8}$$

The resolution of the output value is then given by $p_{\max}/(0.8 \cdot 2^{14}) = 0.8\,\text{mbar}$ for sensor **M** ($0.16\,\text{mbar}$ for sensor **N**).

O   Ambient Pressure and Temperature Sensor

The Bosch BMP280 breakout board is a combined sensor for pressure and temperature. It is used to monitor the ambient conditions. Its pressure range is 0.3 to 1.1 bar and its temperature range is 0 to 65 °C. The data can be read out via the I²C (Inter-Integrated Circuit) serial communication bus. (bought at Berrybase)

P   PT1000 Temperature Sensor Amplifier

A resistance temperature detector PT1000 (**F**) is attached in good thermal contact on the housing of the photomultiplier module. A PT1000 contains a small wire of platinum with a resistance of $1000\,\Omega$ at 0 °C. The resistance has a well known dependence on temperature. A PT1000 RTD Temperature Sensor Amplifier (**P**) with the MAX31865 breakout from Adafruit (product ID: 3648) measures the resistance with high precision. It also includes the possibility to automatically compensate for the resistance of the wires, by using a 4-wire setup in place of just 2 wires. The data is transferred via SPI. (bought at Berrybase and Eckstein)

Q   Analog-to-Digital Converter for the PMT output

The photomultiplier module already incorporates an amplifier, which converts and amplifies the anode current. So the output of the PMT is a coaxial wire with a voltage signal in the order of mV. The high-precision (16-bit) ADS1115 analog-to-digital converter (ADC) breakout board (**Q**) from Adafruit (product ID: 1085) is used to acquire this signal as a digital value. It is used in the differential mode, with one input connected to the inner signal wire and the other connected to the mantel of the coaxial cable. The mantel is grounded on both sides of the cable. All this helps to shield the signal from electromagnetic interference. But additionally, the signal wire is also read out in absolute mode. The included programmable gain amplifier is used to boost the signal another 16 times to get the highest possible resolution. With this configuration, the input range of the ADC is 0 to 256 mV. The ADC makes the signal available via the I²C serial communication bus. (bought at Berrybase)

R   Raspberry Pi Zero

The Raspberry Pi Zero WH is a small low-cost single board computer with 40 input/output pins. These pins are used to connect to the sensors and communicate with them via the SPI or I²C interface (see circuit diagrams in the appendix 7.1). This computer is also able to connect via WiFi and Bluetooth and has a mini-HDMI and micro-B USB port. A second micro-B USB port is used to provide the system with power (5 V). Adapters are used to convert these ports to the larger HDMI and USB-A connectors respectively. The RASPBERRY PI OS LITE (32-bit) operating system is installed on the inserted 32 GB micro-SD card. So this computer runs a complete Linux operating system and can be operated in the console via SSH (Secure Shell Protocol) or a monitor and keyboard. This

makes it possible to program very comfortably in Python.

The Raspberry Pi runs a Python program that collects the data from all the sensors and writes it into a file. The code with detailed comments is shown in the appendix (7.2). At first all necessary python libraries are imported. Except for the Honeywell pressure sensors, all others have their own libraries, which provide functions for easy readout. Then all the sensor are initialised and functions are defined to manually readout and interpret the data from the Honeywell pressure sensors. Following that the data file is opened and a csv-writer is set up. When everything is ready, a infinite loop starts and reads out all the sensor data consecutively and writes the values in the file (see table 3). The time needed for one iteration is $0.156\,\mathrm{s}$, corresponding to a sampling rate of $6.39\,\mathrm{s}^{-1}$. The file is easily accessible saved on the USB stick ($\mathbf{S}$).

Since the Raspberry Pi does not have a power-off button, a program is executed in the background that starts the shutdown process when GPIO pin 4 is connected to ground for at least $3\,\mathrm{s}$. As with all computers, suddenly removing the power supply can damage the system.

variable	column name	unit	sensor	transfer protocol
system date and time	datetime	ISO timestamp		-
ambient temperature	T_bmp	°C	BMP280 ($\mathbf{O}$)	I²C
ambient pressure	P_bmp	mbar		
temperature of PMT	PT1000	°C	PT1000 ($\mathbf{F}$) with ADC ($\mathbf{P}$)	SPI
voltage signal of PMT	V_dif V_A0	mV	PMT with ADC ($\mathbf{Q}$)	I²C
pressure before capillary	P_30	mbar	Honeywell 30psi ($\mathbf{N}$)	SPI
pressure in the minican	P_150	bar	Honeywell 150psi ($\mathbf{M}$)	SPI

Table 3: Compilation of all variables recorded by the program with the unit and name of the column in the data file as well as the corresponding sensor with its transfer protocol.

T-U Power Supply

The old prototype required a power supply of $30\,\mathrm{W}$. By using a modern PMT and omitting its cooling, we were able to reduce the power consumption to less than $3\,\mathrm{W}$. Hence we can use a lightweight ($50\,\mathrm{g}$) rechargeable lithium-polymer battery ($\mathbf{U}$) with $2500\,\mathrm{mA\,h}$ at $3.7\,\mathrm{V}$ and still get a runtime of more than 3 hours. As with the minicans, this is more than enough for an airborne measurement and the battery can easily be swapped for a charged one between flights.

A lithium-polymer battery provides $3.7\,\mathrm{V}$, but the Raspberry Pi and the DC/DC converters for the PMT and the pump need $5\,\mathrm{V}$. Therefore, the PowerBoost 1000 Basic ($\mathbf{T}$) from Adafruit (Product ID: 2030, bought at Berrybase) converts the voltage to the required level. It can be directly connected to the Raspberry PI power port via a USB cable. The DC/DC-converters tap the 5V via the pins of the Raspberry Pi.

Alternatively a normal powerbank can be connected to the Raspberry Pi via the micro-USB port. However, the voltage provided by these is not stable and often too low. The PowerBoost avoids this problem by converting the power to $5.2\,\mathrm{V}$ instead of $5\,\mathrm{V}$. This is within the acceptable range but has a little more 'headroom', so it is less susceptible to voltage drops. A third alternative for laboratory use is to plug the computer via an adaptor directly into a socket.

4   First Test Measurement

In order to carry out calibrations, an ozone generator is available which can produce measuring air with $150\pm3\,\mathrm{ppb}$ ozone mixing ratio. This instrument is used to provide air with a high ozone concentration for the first test of the new prototype. The parameters of this measurement are

- total flow (from pump) $f_{\mathrm{tot}} = 1.66\,\mathrm{l\,min^{-1}} = 27.7\,\mathrm{ml\,s^{-1}}$
- ethylene flow $f_{\mathrm{C_2H_4}} = 0.247\,\mathrm{ml\,s^{-1}}$ $\rightarrow$ ethylene mixing ratio $= 0.9\,\%$
- pressure in minican dropping from 4.27 to $4.09\,\mathrm{bar}$ in $12\,\mathrm{min}$
- pressure before the capillary dropping from 1676 to $1630\,\mathrm{mbar}$ in $12\,\mathrm{min}$
- ambience: pressure $1016.10\pm0.05\,\mathrm{mbar}$, temperature $24.12\pm0.08\,°\mathrm{C}$
- temperature of the PMT: $23.14\pm0.02\,°\mathrm{C}$

The room was completely darkened during operation, because the instrument is extremely sensitive to ambient light, despite the covering of the hoses with black tape.
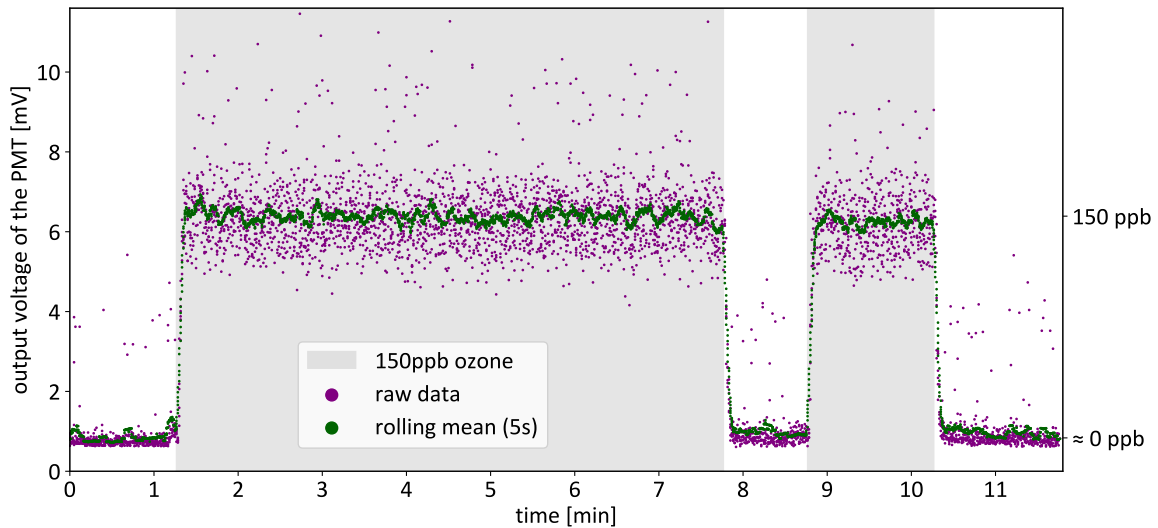

Figure 23: The reaction of the photomultiplier output signal (V_dif, violet) to measuring air with alternating $150\,\mathrm{ppb}$ ozone (from the calibration device) and $0\,\mathrm{ppb}$ (ozone scrubber). The rolling average over 32 raw data points (corresponding to $5\,\mathrm{s}$) is additionally shown in green.

As can be seen in figure 23, the signal from the photomultiplier shows a clear response to changes in ozone mixing ratio. The signal needs at the rising edge about $3\,\mathrm{s}$ and at the falling edge about $4\,\mathrm{s}$ to adjust to this sudden large change in ozone concentration. It is

encouraging that the dark signal (0 ppb ozone) is very small (below 1 mV), despite the relative high room temperature. Unsatisfactorily, the absolute value of the 150 ppb signal is very small and the noise-to-signal ratio is quite high. There are also upward outliers, but these occurred less frequently in other measurements. However, we should be able to significantly improve the quality of the signal by optimising the device parameters, especially the ethylene flow and the gain of the photomultiplier.

Due to the pressure drift in front of the capillary (see chapter 3.3), one would also expect a drift of the ethylene flow and thus of the signal over time. This does not seem to play a significant roll in this dataset. A linear fit to the signal during the first 150 ppb ozone period, results in a slope of $-0.006 \pm 0.010 \, \mathrm{mV \, min^{-1}}$. The fitting error is larger than the value, so the drift of the signal is not significant for this short time span.

5 Conclusion and Outlook

Further measurements of ozone concentration in volcanic plumes are needed. The abundance of SO_2 in the plume causes severe interferences in the usual short wave absorption ozone monitors. Therefore, we constructed and built an ozone monitor based on the chemiluminescence reaction of ozone with ethylene. There is already such an instrument in our research group, but it is very bulky and heavy (about 10 kg). The new prototype should be so lightweight (about 1 kg) that it can be mounted on a small drone to have better access to the plume. The weight reduction was mainly achieved by using a modern photomultiplier module and omitting its cooling. In addition, the battery and ethylene storage container are easy to exchange. This means that they can be quite small, as they only need to last for a few hours at most.

As described in chapter 2, calculations of the photon emission rate and simulations of the photon trajectories were performed. Based on these, the following instrument parameters were chosen in order to maximise the strength of the signal.

- total flow rate $f_{\mathrm{tot}} = 20 \, \mathrm{ml \, s^{-1}}$
- ethylene flow rate $f_{\mathrm{C_2H_4}} = 0.45 \, \mathrm{ml \, s^{-1}}$ $\rightarrow$ ethylene mixing ratio $= 2.25 \, \%$
- cylindrical aluminum reaction chamber:
    - radius $R = 14.25 \, \mathrm{mm}$ fixed by the photomultiplier
    - length $L = 31.35 \, \mathrm{mm}$ $\rightarrow$ volume $V = 20 \, \mathrm{ml}$

The calculation shows that with these parameters for an ozone mixing ratio of 1 ppb (at 10 °C, 1 bar) about 22000 photons per second are emitted by the chemiluminescent reaction. 39 % of these, namely 8400 photons per second reach the photosensitive area of the photomultiplier, resulting in an incidence of $13 \, \frac{\mathrm{photons}}{s \cdot \mathrm{mm^2}}$. We also altered the layout of the gas inlets and outlets in the reaction chamber, in order to improve the detection of the chemiluminescence.

The main work of this thesis was the selection, commission and assembly of the various components of the new prototype. This incorporated the technical design of the reaction

chamber and how it is attached to the photomultiplier. It also involved the soldering of the electrical components onto a circuit board, the setup of the Raspberry Pi computer and writing a program that collects the data from all the different sensors and writes it into a file. Furthermore, several measurements were performed to test different components and study their dependencies.

The relation between temperature and the dark current of the photomultiplier from the old prototype was measured to provide a base for the decision to omit the cooling. An exponential relation was found with a tenfold increase for every $16\,\mathrm{K}$ temperature rise. The different speed of adaptation to the ambient temperature of the photomultiplier and temperature sensor could cause deviations form this relation. So we improved the thermal contact between the sensor and the photomultiplier in the new prototype. Apart from that the relation between the flow generated by the pump and the applied voltage was established. Also, measurements of the temporal evolution of the ethylene supply showed, that the pressure provided by the pressure regulator decreases over time. So the ethylene flow rate is not constant but it has a good linear correlation with the pressure in front of the capillary. We think that with suitable calibration this can be compensated in the post-processing of the data.

A first test measurement of the complete setup demonstrated that the photomultiplier signal shows a clear reaction, if calibration air with a high ozone concentration is applied. However, this first signal was noisy and has a low absolute value. This is mainly because the flow rates were significantly different from the ideal values chosen in chapter 2. Also, the gain of the photomultiplier was not yet at its maximum. The adjustment of these parameters are the next steps.

Then we want to add a small display to enable easy live monitoring of the currently measured values. At the moment the components of the instrument lie loosely on the table, so we need to construct a suitable lightweight housing, probably from styrofoam or similar materials. Especially the elimination of the sensitivity to ambient light is important. The dark current measurements must be repeated for the new photomultiplier to confirm the temperature dependence. Then we need to carry out calibration measurements to establish the relation between the photomultiplier voltage output and the ozone concentrations. This includes corrections for temperature, pressure and ethylene flow variations. Kleindienst et al. (1993) showed that water vapour can have a positive interference on chemiluminescence ozone monitors. This needs to be checked and corrections must also be introduced for this, if necessary.

The calculations in chapter 2.3 showed that the strength of the signal can be more than doubled by increasing the reflectivity of the reaction chamber walls. Therefore, we plan to construct a second reaction chamber that has an inner layer of ODM98 material (diffuse reflectivity $>96\,\%$).

When everything is assembled, test flights with a drone can be carried out. Then the first field measurements of the device will be carried out on Mount Etna.

Acknowledgements

6 References

Atkinson, R., D. L. Baulch, R. A. Cox, J. N. Crowley, R. F. Hampson, R. G. Hynes, M. E. Jenkin, M. J. Rossi, J. Troe, and I. Subcommittee (2006). "Evaluated kinetic and photochemical data for atmospheric chemistry: Volume II - gas phase reactions of organic species". In: *Atmospheric Chemistry and Physics* 6.11, pp. 3625–4055. DOI: 10.5194/acp-6-3625-2006.

Atkinson, R., D. L. Baulch, R. A. Cox, R. F. Hampson, J. A. Kerr, M. J. Rossi, and J. Troe (2000). "Evaluated Kinetic and Photochemical Data for Atmospheric Chemistry: Supplement VIII, Halogen Species Evaluation for Atmospheric Chemistry". In: *Journal of Physical and Chemical Reference Data* 29.2, pp. 167–266. DOI: 10.1063/1.556058.

Birk, M. and G. Wagner (Nov. 2018). "ESA SEOM-IAS – Measurement and ACS database O3 UV region". Version I. In: DOI: 10.5281/zenodo.1485588.

Bobrowski, N., R. von Glasow, A. Aiuppa, S. Inguaggiato, I. Louban, O. W. Ibrahim, and U. Platt (2007). "Reactive halogen chemistry in volcanic plumes". In: *Journal of Geophysical Research: Atmospheres* 112.D6. DOI: 10.1029/2006JD007206.

Burton, M., P. Allard, F. Muré, and A. L. Spina (2007). "Magmatic Gas Composition Reveals the Source Depth of Slug-Driven Strombolian Explosive Activity". In: *Science* 317.5835, pp. 227–230. (Visited on 2022-04-06).

Carn, S. A., K. D. Froyd, B. E. Anderson, P. Wennberg, J. Crounse, K. Spencer, J. E. Dibb, N. A. Krotkov, E. V. Browell, J. W. Hair, G. Diskin, G. Sachse, and S. A. Vay (2011). "In situ measurements of tropospheric volcanic plumes in Ecuador and

Colombia during TC4". In: *Journal of Geophysical Research: Atmospheres* 116.D10. DOI: 10.1029/2010JD014718.

Engineering ToolBox (2018). *Ethylene - Dynamic and Kinematic Viscosity vs. Temperature and Pressure*. [online]. URL: https://www.engineeringtoolbox.com/ethylene-ethene-acetene-C2H4-dynamic-kinematic-viscosity-temperature-pressure-d_2107.html (visited on 2022-05-14).

Finlayson, B. J., J. N. Pitts, and R. Atkinson (1974). "Low-pressure gas-phase ozone-olefin reactions. Chemiluminescence, kinetics, and mechanisms". In: *Journal of the American Chemical Society* 96.17, pp. 5356–5367. DOI: 10.1021/ja00824a009.

Fruchter, J. S., D. E. Robertson, J. C. Evans, K. B. Olsen, E. A. Lepel, J. C. Laul, K. H. Abel, R. W. Sanders, P. O. Jackson, N. S. Wogman, R. W. Perkins, H. H. V. Tuyl, R. H. Beauchamp, J. W. Shade, J. L. Daniel, R. L. Erikson, G. A. Sehmel, R. N. Lee, A. V. Robinson, O. R. Moss, J. K. Briant, and W. C. Cannon (1980). "Mount St. Helens Ash from the 18 May 1980 Eruption: Chemical, Physical, Mineralogical, and Biological Properties". In: *Science* 209.4461, pp. 1116–1125. DOI: 10.1126/science.209.4461.1116.

Gaudel, A., O. R. Cooper, G. Ancellet, B. Barret, A. Boynard, J. P. Burrows, C. Clerbaux, P.-F. Coheur, J. Cuesta, E. Cuevas, S. Doniki, G. Dufour, F. Ebojie, G. Foret, O. Garcia, M. J. Granados-Muñoz, J. W. Hannigan, F. Hase, B. Hassler, G. Huang, D. Hurtmans, D. Jaffe, N. Jones, P. Kalabokas, B. Kerridge, S. Kulawik, B. Latter, T. Leblanc, E. Le Flochmoën, W. Lin, J. Liu, X. Liu, E. Mahieu, A. McClure-Begley, J. L. Neu, M. Osman, M. Palm, H. Petetin, I. Petropavlovskikh, R. Querel, N. Rahpoe, A. Rozanov, M. G. Schultz, J. Schwab, R. Siddans, D. Smale, M. Steinbacher, H. Tanimoto, D. W. Tarasick, V. Thouret, A. M. Thompson, T. Trickl, E. Weatherhead, C. Wespes, H. M. Worden, C. Vigouroux, X. Xu, G. Zeng, and J. Ziemke (May 2018). "Tropospheric Ozone Assessment Report: Present-day distribution and trends of tropospheric ozone relevant to climate and global atmospheric chemistry model evaluation". In: *Elementa: Science of the Anthropocene* 6. 39. DOI: 10.1525/elementa.291.

Gigahertz Optik GmbH (2022). *OP.DI.MA. Diffuse material (ODM)*. URL: https://www.gigahertz-optik.com/en-us/service-and-support/knowledge-base/odm-material-specifications/ (visited on 2022-05-06).

Gutmann, A., N. Bobrowski, T. J. Roberts, J. Rüdiger, and T. Hoffmann (2018). "Advances in Bromine Speciation in Volcanic Plumes". In: *Frontiers in Earth Science* 6. DOI: 10.3389/feart.2018.00213.

Hergert, E. and S. Piatek (2017). *The WITS\$ guide to selecting a photodetector*. Hamamatsu Corporation. URL: https://hub.hamamatsu.com/us/en/technical-notes/detector-selection/the-wits-guide-to-selecting-a-photodetector.html (visited on 2022-05-11).

Hermans, C., A. C. Vandaele, and S. Fally (2009). "Fourier Transform measurements of SO_2 absorption cross sections: I. Temperature dependence in the $23500 - 29000$ cm^{-1} (345-425 nm) region". In: *Journal of Quantitative Spectroscopy and Radiative Transfer* 110, pp. 756–765. DOI: 10.1016/j.jqsrt.2009.01.031.

Hobbs, P. V., J. P. Tuell, D. A. Hegg, L. F. Radke, and M. W. Eltgroth (1982). "Particles and gases in the emissions from the 1980–1981 volcanic eruptions of Mt. St. Helens". In: *Journal of Geophysical Research: Oceans* 87.C13, pp. 11062–11086. DOI: 10.1029/JC087iC13p11062.

Kelly, P. J., C. Kern, T. J. Roberts, T. Lopez, C. Werner, and A. Aiuppa (2013). "Rapid chemical evolution of tropospheric volcanic emissions from Redoubt Volcano, Alaska, based on observations of ozone and halogen-containing gases". In: *Journal of Volcanology and Geothermal Research* 259. The 2009 Eruption of Redoubt Volcano, Alaska, pp. 317–333. DOI: 10.1016/j.jvolgeores.2012.04.023.

Kleindienst, T. E., E. E. Hudgens, D. F. Smith, F. F. McElroy, and J. J. Bufalini (1993). "Comparison of Chemiluminescence and Ultraviolet Ozone Monitor Responses in the Presence of Humidity and Photochemical Pollutants". In: *Air & Waste* 43.2, pp. 213–222. DOI: 10.1080/1073161X.1993.10467128.

Kochanov, R. V., I. E. Gordon, L. S. Rothman, K. P. Shine, S. W. Sharpe, T. J. Johnson, T. J. Wallington, J. J. Harrison, P. F. Bernath, M. Birk, G. Wagner, K. L. Bris, I. Bravo, and C. Hill (2019). "Infrared absorption cross-sections in HITRAN2016 and beyond: Expansion for climate, environment, and atmospheric applications". In: *Journal of Quantitative Spectroscopy and Radiative Transfer*. DOI: 10.1016/j.jqsrt.2019.04.001.

Lee, C., Y. J. Kim, H. Tanimoto, N. Bobrowski, U. Platt, T. Mori, K. Yamamoto, and C. S. Hong (2005). "High ClO and ozone depletion observed in the plume of Sakurajima volcano, Japan". In: *Geophysical Research Letters* 32.21. DOI: 10.1029/2005GL023785.

Leston, A. R., W. M. Ollison, C. W. Spicer, and J. Satola (2005). "Potential Interference Bias in Ozone Standard Compliance Monitoring". In: *Journal of the Air & Waste Management Association* 55.10, pp. 1464–1472. DOI: 10.1080/10473289.2005.10464749.

Oppenheimer, C., P. Kyle, F. Eisele, J. Crawford, G. Huey, D. Tanner, S. Kim, L. Mauldin, D. Blake, A. Beyersdorf, M. Buhr, and D. Davis (2010). "Atmospheric chemistry of an Antarctic volcanic plume". In: *Journal of Geophysical Research: Atmospheres* 115.D4. DOI: 10.1029/2009JD011910.

Parrish, D. D. and F. C. Fehsenfeld (2000). "Methods for gas-phase measurements of ozone, ozone precursors and aerosol precursors". In: *Atmospheric Environment* 34.12, pp. 1921–1957. DOI: 10.1016/S1352-2310(99)00454-9.

photonis (n.d.). *Photomultiplier tube basics*. URL: https://psec.uchicago.edu/librar y/photomultipliers/Photonis_PMT_basics.pdf (visited on 2022-05-12).

Platt, U. and N. Bobrowski (2015). "Quantification of volcanic reactive halogen emissions". In: pp. 115–132. DOI: 10.1017/CBO9781107415683.011.

Platt, U. and E. Lehrer (1996). *Arctic tropospheric ozone chemistry, ARCTOC, Final Report of the EU-Project No.* Tech. rep. EV5V-CT93-0318, Heidelberg.

Roberts, T. J. (2018). "Ozone Depletion in Tropospheric Volcanic Plumes: From Halogen-Poor to Halogen-Rich Emissions". In: *Geosciences* 8.2. DOI: 10.3390/geosciences802 0068.

Rüth, M. (2021). "Characterisation of a chemiluminescence ozone monitor for volcanic applications". Heidelberg: Bachelor thesis, University Heidelberg, under the supervision of U. Platt. DOI: 10.11588/heidok.00029947.

Surl, L., D. Donohoue, A. Aiuppa, N. Bobrowski, and R. von Glasow (2015). "Quantification of the depletion of ozone in the plume of Mount Etna". In: *Atmospheric Chemistry and Physics* 15.5, pp. 2613–2628. DOI: 10.5194/acp-15-2613-2015.

Vance, A., A. J. S. McGonigle, A. Aiuppa, J. L. Stith, K. Turnbull, and R. von Glasow (2010). "Ozone depletion in tropospheric volcanic plumes". In: *Geophysical Research Letters* 37.22. DOI: 10.1029/2010GL044997.

von Glasow, R., N. Bobrowski, and C. Kern (2009). "The effects of volcanic eruptions on atmospheric chemistry". In: *Chemical Geology* 263.1. Halogens in Volcanic Systems and Their Environmental Impacts, pp. 131–142. DOI: 10.1016/j.chemgeo.2008.08.020.

Wagner, T. and U. Platt (1998). "Satellite mapping of enhanced BrO concentrations in the troposphere". In: *Nature* 395, pp. 486–490. DOI: 10.1038/26723.

Williams, E. J., F. C. Fehsenfeld, B. T. Jobson, W. C. Kuster, P. D. Goldan, J. Stutz, and W. A. McClenny (2006). "Comparison of Ultraviolet Absorbance, Chemiluminescence, and DOAS Instruments for Ambient Ozone Monitoring". In: *Environmental Science & Technology* 40.18, pp. 5755–5762. DOI: 10.1021/es0523542.

Zahn, A., J. Weppner, H. Widmann, K. Schlote-Holubek, B. Burger, T. Kühner, and H. Franke (2012). "A fast and precise chemiluminescence ozone detector for eddy flux and airborne application". In: *Atmospheric Measurement Techniques* 5.2, pp. 363–375. DOI: 10.5194/amt-5-363-2012.
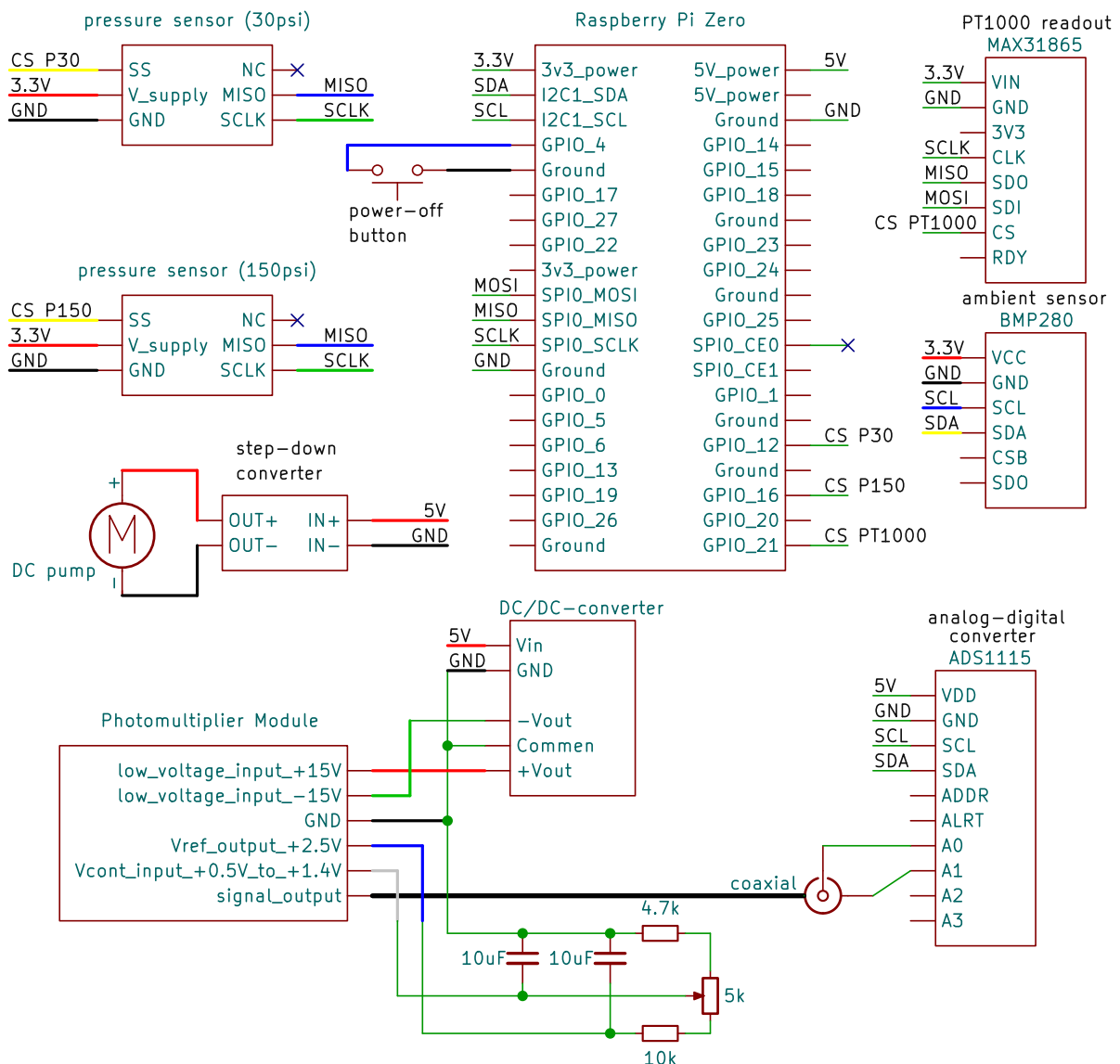
7 Appendix

7.1 Circuit Diagram

Figure 24: Circuit diagram of the electronics of the new chemiluminescence ozone monitor. The power is provided via the Raspberry Pi, which is supplied from a battery with a USB cable. So the `3V3_power` and `5V_power` pins of the Raspberry Pi are the power source in this diagram. The colour of the line indicates the color of the real wire, if applicable.

7.2 Data Logging Code

```
## IMPORT NECESSERY LIBRARYS
# for reading out the the system time and date
from datetime import datetime

# for writing directly csv-files (comma-seperated value)
import csv

# for acessing the serial interfaces of the RPi (SPI, I2C)
import board
```

```python
# for the BMP280 ambient temperature and pressure sensor
from bmp280 import BMP280
from smbus2 import SMBus

#for the PT1000 (MAX31865)
import adafruit_max31865
import digitalio

#for the ADC (PMT read out) (ADS1115)
import busio
import adafruit_ads1x15.ads1115 as ADS
from adafruit_ads1x15.analog_in import AnalogIn

#for the Honeywell pressure sensors
import spidev #general purpuse SPI library
import RPi.GPIO as gpio #access to the GPIO pins (general purpos input output)

## INITIALSE THE SENSORS
# BMP280
bus = SMBus(1)
bmp280 = BMP280(i2c_dev=bus)

# PT1000
spi = board.SPI()
# Choose which pin (PIN 21) is the Chip Select for the MAX31865 board.
cs = digitalio.DigitalInOut(board.D21)
PT1000 = adafruit_max31865.MAX31865(spi, cs, wires=4, rtd_nominal=1000.0,
    ref_resistor=4300.0) # pass the set-up parameters of the PT1000

# ADC
i2c = busio.I2C(board.SCL, board.SDA)
ads = ADS.ADS1115(i2c)
ads.gain = 16 # =1,2,4,8,16; specify gain for the programable gain amplifier
# define the channel in differential mode (with input pins 0 and 1)
chan_dif = AnalogIn(ads, ADS.P0, ADS.P1)
# additional channel in single mode, reading out the PMT signal wire directly
chan_ana = AnalogIn(ads, ADS.P0)

# pressure sensors
# The RPi has only 2 pins directly dedicated as chip selects for SPI, so the
# chip select (CS) pins for the pressure sensor are turned on and off manually
pin30 = 12 # CS-pin for 30psi pressure sensor
pin150 = 16 # CS-pin for 150psi pressure sensor
gpio.setup(pin30, gpio.OUT)
gpio.setup(pin150, gpio.OUT)
gpio.output(pin30, gpio.HIGH) # set the CS pins initally to high
gpio.output(pin150, gpio.HIGH)

P_spi=spidev.SpiDev() # initialize SPI bus for the pressure sensors
P_spi.open(0,0)        # SPI connection with bus 0 and CS-pin CE0 (= GPIO 8, pin
    24); this CS-pin is turned on and off, but no slave is connected there
P_spi.max_speed_hz = 15200

# Define the funcions needed to read out the pressure sensors
def get_pressure(pin, P_max):
  gpio.output(pin, gpio.LOW) # set CS-pin low -> associated slave is adressed
  high, low = P_spi.xfer2([0,0]) # raw read out from the pressure sensor
  gpio.output(pin, gpio.HIGH) # set CS-pin high again -> stop adressing slave
  count = high*2**8+low # convert read out to number (between 0 and 2^14)
  # formula to convert output number to pressure (see chapter 3.4 M N)
  pressure = (count-0.1*2**14)*P_max/(0.8*2**14)
  return pressure
def getP30():
  Pmax30 = 2068.43 #mbar, = 30 psi
  pressure = get_pressure(pin30, Pmax30)
  return pressure
def getP150():
  Pmax150 = 10.3421 #bar, = 150 psi
  pressure = get_pressure(pin150, Pmax150)
  return pressure
```

```python
# open the file on the USB stick
# "a" - Append - Opens file for appending, creates the file if not existing
with open("/media/usbstick/ozon-daten.txt", "a", newline='') as f:
  # initialize the csv writer (with tabs between values)
  writer = csv.writer(f, delimiter='\t')
  writer.writerow(['datetime', 'T_bmp', 'P_bmp', 'PT1000', 'V_dif', 'V_A0', '
    P_30', 'P_150']) # write header line
  #repeat as fast as possible until the program is interupted: read out all the
    sensors and write it into the file
  while (True):
    writer.writerow([datetime.now(),        # ISO-timestamp
      f'{bmp280.get_temperature():.3f}', # degree Celsius (ambient temperature)
      f'{bmp280.get_pressure():.3f}',    # mbar (ambient pressure)
      f'{PT1000.temperature:.2f}',       # degree Celsius (temperature of PMT)
      f'{chan_dif.voltage*1000:.2f}',    # mV (readout of PMT, difference mode)
      f'{chan_ana.voltage*1000:.2f}',    # mV (readout of PMT, single mode)
      f'{getP30():.1f}',                 # mbar (pressure in front of capillary)
      f'{getP150():.4f}'])               # bar (pressure in the minican)
    f.flush() # update file, otherwise data gets lost when program is interupted
```

7.3 Data Sheets

(visited on 2022-05-22)

Photosensor Module H10493-001 from Hamamatsu Photonics GmbH:
  http://www.hamamatsu.com/content/dam/hamamatsu-photonics/sites/documents/99_SALES_LIBRARY/etd/m-h10493e.pdf

Pump model G 6/01-K-LC 1 from Thomas by Gardner Denver:
  http://www.usathomas.com/assets/images/Rotary_vane_mini_pumps-2.pdf (page 3)

Mini pressure regulator model 638.42 from filcom and HUG-technik:
  https://www.filcom-technik.de/media/catalog/download/de/wartungsgeraete/Technische_Daten_Mini_Druckregler_00045278_0.pdf

Pressure sensors ABPDANV150PGSA3 and ABPDANV030PGSA3 from Honeywell:
  https://prod-edam.honeywell.com/content/dam/honeywell-edam/sps/siot/en-us/products/sensors/pressure-sensors/board-mount-pressure-sensors/basic-abp-series/documents/sps-siot-basic-board-mount-pressure-abp-series-datasheet-32305128-ciid-155789.pdf

Analog-to-digital-converter ADS1115 from Adafruit:
  https://learn.adafruit.com/adafruit-4-channel-adc-breakouts

PT1000 temperature sensor amplifier MAX31865 from Adafruit:
  https://learn.adafruit.com/adafruit-max31865-rtd-pt100-amplifier

Ambient pressure and temperature sensor, Bosch BMP280 from Berrybase:
  https://www.berrybase.de/Pixelpdfdata/Articlepdf/id/6008/onumber/GY-BMP280

PowerBoost 1000 basic from Adafruit:
  https://learn.adafruit.com/adafruit-powerboost-1000-basic

Mini step-down converter (for pump) from sertronics:
  https://www.berrybase.de/Pixelpdfdata/Articlepdf/id/6782/onumber/REGA3A

DC/DC-converter TMA 0515D (for PMT) from TracoPower:
  https://asset.conrad.com/media10/add/160267/c1/-/en/000154158DS02/datenblatt-154158-tracopower-tma-0512d-dcdc-wandler-print-5-vdc-12-vdc-12-vdc-40-ma-1-w-anzahl-ausgaenge-2-x.pdf

Erklärung

Ich versichere, dass ich diese Arbeit selbstständig verfasst und keine anderen als die angegebenen Quellen und Hilfsmittel benutzt habe.

Heidelberg, den ..., 26.05.2022